Generalized spin kitten states in a strongly coupled spin-oscillator system

M. Balamurugan,[1] R. Chakrabarti,[1] B. Virgin Jenisha,[1,2] and V. Yogesh[1,3]
[1]*Department of Theoretical Physics, University of Madras, Guindy Campus, Chennai 600 025, India*
[2]*Department of Physics, Government College of Engineering, Srirangam, Tamil Nadu 620 012, India*
[3]*Department of Theoretical Sciences, S.N. Bose National Centre for Basic Sciences, Block-JD, Sector-III, Salt Lake, Kolkata 700 106, India*

(Received 6 May 2020; revised 21 April 2021; accepted 27 April 2021; published 3 June 2021)

Utilizing an adiabatic approximation method, a bipartite qudit-oscillator Hamiltonian is studied for low-spin values in both strong and ultrastrong coupling regimes. The quasiprobability densities on the hybrid factorized phase space are introduced. Integrating over a sector of the composite phase space, the quasiprobability distributions of its complementary subsystem are recovered. In the strong coupling regime, the qudit entropy displays a pattern of quasiperiodic collapses and revivals, where the latter coincide with locally minimum entropy configurations. Starting with a bipartite factorizable initial state, we observe that almost pure spin kitten type states dynamically develop at near-null values of entropy. The Hilbert-Schmidt distance measure of these states puts them metrically far away from the initial state. Other localized spin states form at locally minimum but significantly large values of entropy. The evolution to the nonclassical transitory spin states is displayed via the diagonal spin P_Q representation. As another manifestation of nonclassicality the emergence of the spin-squeezed states during the bipartite evolution is observed. In the ultrastrong coupling domain, a large number of interaction-dependent modes and their harmonics are generated. The consequent randomization of the phases eliminates the quasiperiodicity of the system which is now driven towards a stabilization of the entropy that also undergoes stochastic fluctuations around a suitably stabilized value. In both the strong and ultrastrong coupling realms, antibunching of the photoemission events is realized particularly for the small spin values.

DOI: 10.1103/PhysRevA.103.063703

I. INTRODUCTION

Recently, much interest has developed towards experimental and theoretical studies on hybrid interacting spin-oscillator systems going beyond the rotating-wave approximation [1] that complies with the preservation of the total excitation number. While the said approximation remains valid in a weak coupling regime endowed with a small detuning between the spin and the oscillator frequencies, recent experimental realizations use a varied set of tools to explore systems with strong and ultrastrong coupling between the degrees of freedom. For instance, a nanoelectromechanical resonator capacitively coupled to a Cooper pair box driven by microwave currents [2,3], a flux-biased quantum circuit that utilizes the large inductance of a Josephson junction to generate an ultrastrong coupling with a coplanar waveguide resonator [4,5], and a quantum semiconductor microcavity embedding doped quantum wells [6,7] lie in this category. Specifically, the superconducting two-level (qubit) as well as multilevel (qudit) systems and circuits acting as artificial atoms are adaptable for a wide range of parameters. This flexibility makes them the preferred building blocks for quantum simulators [8–14]. Multilevel superconducting circuit has been recently considered [15] for implementing quantum gates. In principle, the entangled multilevel quantum systems store significantly more information, and have less networking problems compared to their two-level counterparts. An experimental demonstration of the nonclassical properties of a photonic qudit state has been achieved [16]. Moreover, hybrid quantum circuits integrating multilevel atoms, spins, cavity photons, and superconducting qudits coupled with nanoelectromechanical resonators hold much promise for realization of the quantum information network [17].

On the other hand, the atomic coherent state [18,19] provides a description for the collective atomic quantum processes such as superradiance [20–22] and resonance fluorescence [23,24] that require quantum correlations in an atomic ensemble. One crucial instance of nonclassical properties is evident in the formation of the Schrödinger cat and kitten states [25] that embody a coherent superposition of two or more distinguishable states of a macroscopic system. These states have been studied [26] in an ensemble of two-level atoms interacting with a dispersive cavity mode in the context of the rotating-wave approximation. Atomic cat-type states are known [27] to display interference-induced properties such as enhancement or reduction in the rates of spontaneous and stimulated emission. Employing two hyperfine ground states of a beryllium ion, the authors of Ref. [28] considered a collection of ions confined in an electromagnetic trap and controlled with a classical laser beam. The cat states representing equal superposition of two maximally distinct states have been observed [28] up to six ions. A probabilistic scheme has been proposed [29] for obtaining pure entangled spin states in large atomic ensembles where the transmitted photons undergo a weak random Faraday rotation caused by the quantum noise of the atomic spin. Two or more photons

emerging from the system with their polarization vectors orthogonal to the corresponding incoming polarization direction signal formation [29] of atomic Schrödinger cat states. Experimental realization of atomic cat states characterized by coherent superposition of electronic spin states of opposite orientation has been observed [30] in samples of dysprosium atoms undergoing ac Stark shift effected by detuned spin-light interaction. More recently, using superconducting transmon qubits coupled via a coplanar waveguide bus resonator, the authors of Ref. [31] constructed Schrödinger kitten states consisting up to 20 qubits.

Another feature of nonclassicality is expressed by the spin-squeezed states [32–34], which owe their origin to the nonlinear spin-spin effective interaction in the theory. These states have been extensively utilized in the study of quantum phase transitions [35,36], quantum chaos [37], Bose-Einstein condensate [38,39], and arrays of superconducting qubits [40,41]. Recently, one photon–two atom excitation process has been considered [42] towards engendering optimal squeezing in an ensemble of N spins coupled to a single cavity mode. The spin-squeezed state improves the precision measurement of magnetometry beyond the standard quantum limit [43]. Interestingly, employing the quantum state transfer from the nonclassical light to the cold atoms, the generation of macroscopic spin-squeezed ensemble of atoms has been experimentally observed [44]. An extensive recent review of the spin squeezing is given in Ref. [45].

In the setting described above, here we study the evolution of a hybrid bipartite state which is a linear combination of the qudit spin coherent states tensored with the squeezed coherent states of the field mode. A suitable adiabatic approximation pioneered in Refs. [46,47] allows us to investigate the combined structure for a strong spin-photon coupling as well as a large detuning of the associated frequencies. To analyze the system, we introduce the bipartite quasiprobability distributions in the composite phase space of the qudit and field variable. Tracing over one degree of freedom reproduces the phase-space quasiprobability distributions [48–50] of the coupled complementary subsystem. Starting with a factorized state of the bipartite system in the strong interaction regime, nonclassical configurations such as the transitory generalized qudit kitten states dynamically emerge corresponding to the near-null values of entropy arrived at suitable local minima of its time evolution. The almost pure generalized spin kitten states, while maintaining large Hilbert-Schmidt distance from the initial state, incorporate superposition of an appropriately small number of spin coherent states. We also employ a tomographic procedure towards reproducing the states of the qudit by utilizing the close kinship between the quasiprobability distributions and the probability densities related to the diagonal elements of the spin density matrix in an arbitrarily rotated frame [51,52]. The transient spin kitten type states are also evident in the tomographic depictions considered here. Moreover, quantum fluctuations triggered by the nonlinear terms in the effective Hamiltonian of the spin degree of freedom turn spin coherent states to short-lived squeezed-spin states. Towards illustrating the above construction, we explicitly discuss the low spin $s = 1, \frac{3}{2}$ cases. For a higher-spin variable, more complex kitten type states emerge as a larger Hilbert space allows for superposition involving more state vectors. We also investigate the ultrastrong spin-oscillator coupling regime where the said adiabatic approximation [46,47] is found to remain valid. In this domain, the realization of a large number of interaction modes spread over a wide range of timescales abolishes the phase correlations necessary for the manifestation of the generalized spin kitten states, which, as a consequence, disappear. In addition, it causes the materialization of a steady-state value of the entropy, which is, however, subjected to rapid stochastic fluctuations.

II. HAMILTONIAN AND ITS APPROXIMATE DIAGONALIZATION

The bipartite qudit-oscillator Hamiltonian reads as

$$H = -\Delta S_{\mathsf{x}} + \omega a^{\dagger} a + \lambda S_{\mathsf{z}}(a + a^{\dagger}). \tag{2.1}$$

The spin variables $\{S_{\mathcal{X}} | \mathcal{X} = \mathsf{x}, \mathsf{y}, \mathsf{z}\}$ obey the su(2) algebra $\{S_{\pm} \equiv S_{\mathsf{x}} \pm i S_{\mathsf{y}}; [S_z, S_{\pm}] = \pm S_{\pm}, [S_+, S_-] = 2S_{\mathsf{z}}\}$ and maintain the standard irreducible representations

$$\begin{aligned} S_{\mathsf{z}}|s, m\rangle &= m|s, m\rangle, \\ S_{\pm}|s, m\rangle &= \sqrt{(s \mp m)(s \pm m + 1)}\,|s, m \pm 1\rangle; \\ s &= 0, \tfrac{1}{2}, 1, \ldots; \; m = -s, -s+1, \ldots, s, \end{aligned} \tag{2.2}$$

whereas the oscillator degree of freedom is characterized as follows: $\{a, a^{\dagger}, \hat{n} \equiv a^{\dagger} a; [a, a^{\dagger}] = \mathbb{I} : \hat{n}|n\rangle = n|n\rangle, a|n\rangle = \sqrt{n}\,|n-1\rangle, a^{\dagger}|n\rangle = \sqrt{n+1}\,|n+1\rangle\}$. Employing a variational method, the Hamiltonian (2.1) has been previously investigated, and in the vicinity of the resonance configuration its approximate ground state has been determined [53]. On the other hand, the adiabatic approximation [46,47] considered here employs a separation of the timescales between the fast-moving oscillator with frequency ω, and the slow-moving qudit possessing an energy gap $\Delta \ll \omega$. The qudit-oscillator coupling is parametrized by λ. The strong and ultrastrong interaction regimes $\lambda \lesssim \omega$ necessitate incorporating terms in the Hamiltonian (2.1) that do not preserve the excitation number. Under the said approximation the high-frequency oscillator instantaneously adjusts to the eigenstate of the qudit operator S_{z} and, consequently, it is subjected to the Hamiltonian

$$H_{\mathcal{O}} = \omega a^{\dagger} a + \lambda\, m\, (a + a^{\dagger}), \quad \langle s, m|\, S_{\mathsf{z}}\, |s, m\rangle = m. \tag{2.3}$$

The eigenenergies and the corresponding diagonalizing states of the oscillator Hamiltonian $H_{\mathcal{O}}$ read as

$$\varepsilon_{n,m} = \omega[n - (m\widetilde{\lambda})^2], \quad \widetilde{\lambda} = \tfrac{\lambda}{\omega}, \quad |n_m\rangle = \mathrm{D}(m\widetilde{\lambda})^{\dagger}|n\rangle, \tag{2.4}$$

where the displacement operator is denoted by $\mathrm{D}(\alpha) = \exp(\alpha a^{\dagger} - \alpha^* a)$, $\alpha = \mathrm{Re}(\alpha) + i\,\mathrm{Im}(\alpha)$. Mimicking the construction in [46], a matrix representation of the Hamiltonian (2.1) in the complete basis set $|s, m\rangle|n_m\rangle \equiv |s, m; n_m\rangle$ may be furnished. The nonvanishing overlap between the basis vectors causes this matrix to be infinite dimensional that may be approximately diagonalized only numerically. Under the adiabatic approximation, however, the Hamiltonian H assumes a block-diagonal form where the nth photonic manifold is expressed via the basis set $|s, m; n_m\rangle$. The approximation utilizes [46] the self-energy of the spin degree of freedom just to eliminate the degeneracy evident in the displaced oscillator representation (2.4). Effectively it leads to a mixing between the states $|n_m\rangle$ for a fixed value of n. The approximate energy

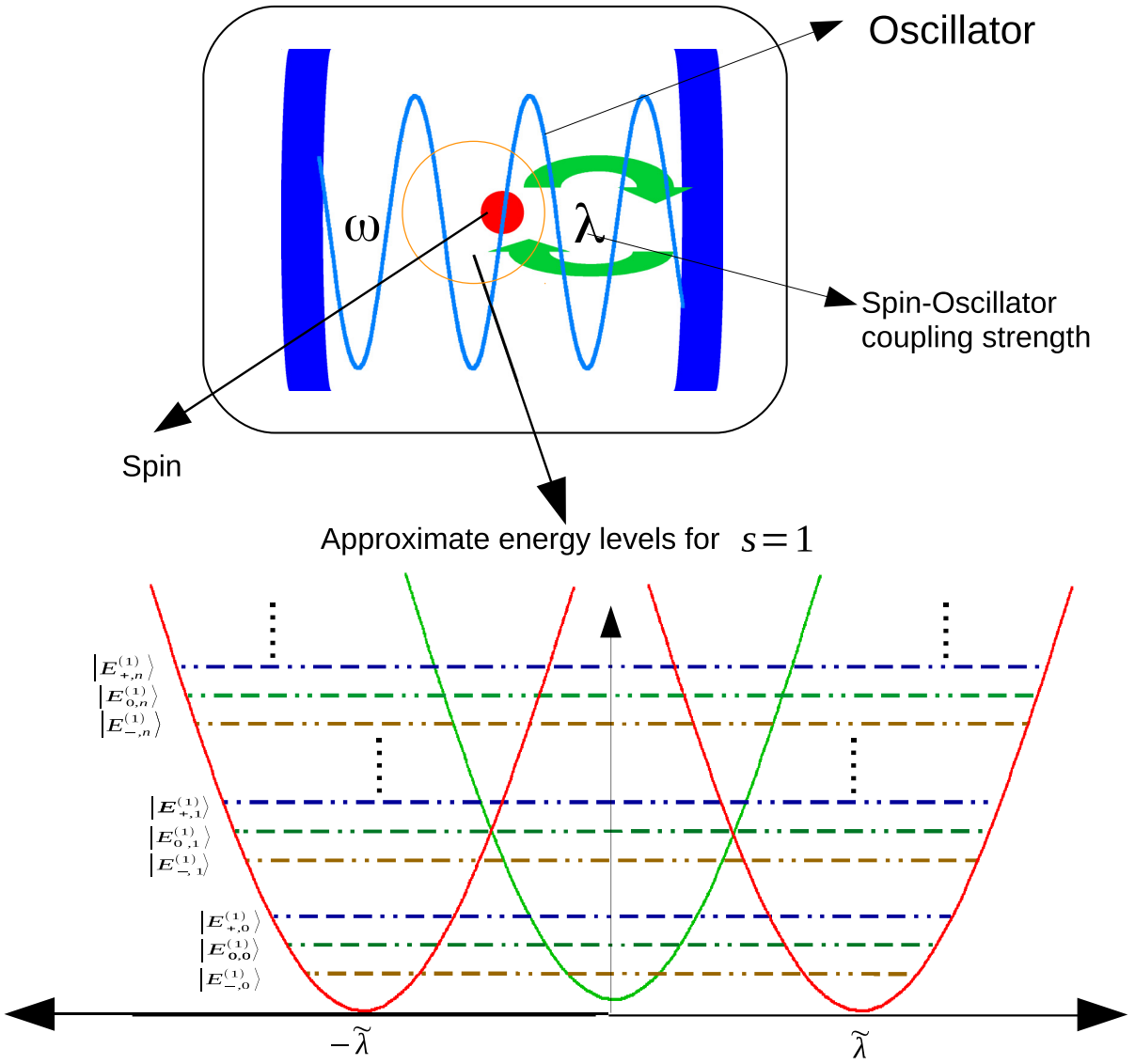

FIG. 1. The cavity mode and the spin constitute the interacting system which is diagonalized in a displaced operator basis. The harmonic-oscillator well is shifted by an amount proportional to the spin quantum number m. The adiabatic approximation permits block diagonalization of the Hamiltonian. A representational view of the eigenstates of the nth manifold is shown.

eigenstates for the said nth photonic manifold in the examples of spin variables $s = 1, \frac{3}{2}$ are described in this work. A schematic view of the approximate diagonalization of the interacting Hamiltonian for the $s = 1$ case is given in Fig. 1.

For the $s = 1$ case, the nth photonic block of the Hamiltonian is given by

$$H_n^{(s=1)} = \omega \begin{pmatrix} n-\widetilde{\lambda}^2 & \Delta_n & 0 \\ \Delta_n & n & \Delta_n \\ 0 & \Delta_n & n-\widetilde{\lambda}^2 \end{pmatrix}, \tag{2.5}$$

where the scaled and renormalized qudit gap parameter is listed as $\Delta_n = -\frac{\Delta}{\sqrt{2}\omega}\exp(-\frac{\widetilde{\lambda}^2}{2})L_n^0(\widetilde{\lambda}^2)$. The Laguerre polynomial maintains the standard expansion $L_n^k(\mathsf{x}) = \sum_\ell \frac{(-1)^\ell}{\ell!}\binom{n+k}{n-\ell}\mathsf{x}^\ell$. In the subspace of the nth block the eigenenergies $E^{(1)}_{J,n}$, $J \in \{0, \pm\}$ of the Hamiltonian (2.5) may be given by

$$E^{(1)}_{0,n} = \omega(n-\widetilde{\lambda}^2), \quad E^{(1)}_{\pm,n} = \omega\big[n - \tfrac{1}{2}(\widetilde{\lambda}^2 \mp \delta_n)\big],$$
$$\delta_n = \sqrt{8\Delta_n^2 + \widetilde{\lambda}^4} \tag{2.6}$$

and the corresponding normalized eigenvectors read as

$$|E^{(1)}_{0,n}\rangle = \frac{1}{\sqrt{2}}(|1,1;n_1\rangle - |1,-1;n_{-1}\rangle),$$
$$|E^{(1)}_{\pm,n}\rangle = \frac{1}{\sqrt{\mathcal{N}^{(1)}_{\pm,n}}}[2\Delta_n|1,1;n_1\rangle + (\widetilde{\lambda}^2 \pm \delta_n)|1,0;n\rangle + 2\Delta_n\,|1,-1;n_{-1}\rangle],$$
$$\mathcal{N}^{(1)}_{\pm,n} = 2\delta_n(\delta_n \pm \widetilde{\lambda}^2). \tag{2.7}$$

In a specific nth-photonic block, the above basis set fulfills the orthocompleteness relations $\langle E^{(1)}_{J,n}|E^{(1)}_{\ell,n}\rangle = \delta_{J\ell}$, where

$\jmath, \ell \in \{0, \pm\}$, and $\sum_{\jmath} |E^{(1)}_{\jmath,n}\rangle\langle E^{(1)}_{\jmath,n}| = \mathbb{I}$. The energies (2.6) and the related states (2.7) constitute the lowest-order adiabatic approximation in the manner of [46,47] for the $s = 1$ qudit. Moreover, the approximate energy eigenstates constructed herein [Eqs. (2.7) and (B3)] are also eigenstates of the conserved parity operator: $\mathcal{P} = \exp[i\pi(a^\dagger a + \frac{1}{2}\,\mathfrak{r} + S_{\mathsf{x}})]$, where the index reads as $\mathfrak{r} = 0\,(1)$ for integral (half-integral) values of the spin s.

III. INITIAL STATE AND ITS EVOLUTION VIA THE ADIABATIC APPROXIMATION

The generalized quasi-Bell bipartite entangled initial state is chosen as

$$|\psi_s(0)\rangle = \mathcal{N}_s(|\mathfrak{z}\rangle_{(s)}\ \ |\alpha, \xi\rangle + \mathrm{c}\,|-\mathfrak{z}\rangle_{(s)}\ \ |-\alpha, \xi\rangle), \tag{3.1}$$

where $|\mathfrak{z}\rangle_{(s)}$ is the qudit spin-s coherent state [19]. Its expansion via the eigenstates of the generator S_{z} reads as

$$|\mathfrak{z}\rangle_{(s)} = \frac{1}{(1+|\mathfrak{z}|^2)^s} \sum_{m=-s}^{s} \binom{2s}{s+m}^{\frac{1}{2}} \mathfrak{z}^{s+m}\,|s, m\rangle. \tag{3.2}$$

The polar coordinate $[\mathfrak{z} = \tan(\frac{\widetilde{\theta}}{2})\,\exp(-i\widetilde{\phi})]$ allows us to recast the sum (3.2) in terms of the spherical phase-space variables as

$$|\mathfrak{z}\rangle_{(s)} \equiv |\widetilde{\theta}, \widetilde{\phi}\rangle_{(s)} = \sum_{m=-s}^{s} \binom{2s}{s+m}^{\frac{1}{2}} \left(\sin\frac{\widetilde{\theta}}{2}\right)^{s+m} \left(\cos\frac{\widetilde{\theta}}{2}\right)^{s-m} \exp[-i(s+m)\widetilde{\phi}]\,|s, m\rangle. \tag{3.3}$$

The squeezed oscillator coherent state [50] is structured as $|\alpha, \xi\rangle \equiv \mathrm{D}(\alpha)\mathrm{S}(\xi)|0\rangle$, $\mathrm{S}(\xi) = \exp(\frac{\xi^* a^2 - \xi a^{\dagger 2}}{2})$, where $\xi[= r\,\exp(i\zeta)] \in \mathbb{C}$. Employing the parameters $\mu = \cosh r$, $\nu = \sinh r\,\exp(i\zeta)$ its mode expansion is given by

$$|\alpha, \xi\rangle = \sum_{n=0}^{\infty} \mathcal{S}_n(\alpha, \xi)|n\rangle, \quad \mathcal{S}_n(\alpha, \xi) = \frac{1}{\sqrt{n!\,\mu}} \left(\frac{\nu}{2\mu}\right)^{\frac{n}{2}} \exp\left(-\frac{1}{2}\,|\alpha|^2 - \frac{\nu}{2\,\mu}\,\alpha^{*2}\right) \mathrm{H}_n\left(\frac{\mu\alpha + \nu\alpha^*}{\sqrt{2\,\mu\,\nu}}\right), \tag{3.4}$$

where the Hermite polynomials obey the sum rule $\exp(2\mathcal{X}t - t^2) = \sum_{n=0}^{\infty} H_n(\mathcal{X})\,\frac{t^n}{n!}$. For a large value of the parameter $|\alpha|^2 \gg 1$ the oscillator coherent state may be regarded as macroscopic in nature. The normalization constant for the initial state (3.1) reads as $\mathcal{N}_s = [1 + |\mathrm{c}|^2 + 2(\frac{1-|\mathfrak{z}|^2}{1+|\mathfrak{z}|^2})^{2s} \exp(-2|\alpha\mu + \alpha^*\nu|^2)\ \mathrm{Re}\,(\mathrm{c})]^{-\frac{1}{2}}$. The parameter $\mathrm{c} \in \mathbb{C}$ appearing in the linear combination (3.1) allows us to suitably select the initial state. For instance, the choice $\mathrm{c} = 0$ leads to the factorized bipartite state at $t = 0$, and therefore the transient formation of the nonclassical states discussed in Sec. VI owes its origin to dynamical effects.

For the spin $s = 1$ case our approximate diagonalization via the basis states $\{|E^{(1)}_{\jmath,n}\rangle\,|\jmath \in (0, \pm); n = 0, 1, \ldots\}$ given in (2.7) permits us to extract the time evolution of the corresponding initial state (3.1):

$$|\psi_{_1}(t)\rangle = \sum_{\jmath} \sum_{n=0}^{\infty} \mathcal{A}^{(1)}_{\jmath,n}\ \exp\big(-iE^{(1)}_{\jmath,n}t\big)\ \big|E^{(1)}_{\jmath,n}\big\rangle, \tag{3.5}$$

where the projectors of the initial state (3.1) on the approximate eigenvector basis (2.7) read as

$$\begin{aligned}
\mathcal{A}^{(1)}_{0,n} &\equiv \big\langle E^{(1)}_{0,n}\big|\psi_{_1}(0)\big\rangle = \frac{\mathcal{N}_1}{\sqrt{2}\,(1+|\mathfrak{z}|^2)}([\mathfrak{z}^2 - (-1)^n\mathrm{c}]\,\exp[-i\widetilde{\lambda}\,\mathrm{Im}(\alpha)]\,\mathcal{S}_n(\alpha_+, \xi) - [1 - (-1)^n\mathrm{c}\,\mathfrak{z}^2]\exp[i\widetilde{\lambda}\,\mathrm{Im}(\alpha)]\,\mathcal{S}_n(\alpha_-, \xi)),\\
\mathcal{A}^{(1)}_{\pm,n} &\equiv \big\langle E^{(1)}_{\pm,n}\big|\psi_{_1}(0)\big\rangle = \frac{\mathcal{N}_1}{\sqrt{\mathcal{N}^{(1)}_{\pm,n}\,(1+|\mathfrak{z}|^2)}}(2\Delta_n\,[\mathfrak{z}^2 + (-1)^n\mathrm{c}]\,\exp[-i\widetilde{\lambda}\mathrm{Im}(\alpha)]\,\mathcal{S}_n(\alpha_+, \xi) + \sqrt{2}(\widetilde{\lambda}^2 \pm \delta_n)\,\mathfrak{z}\,[1 - (-1)^n\mathrm{c}]\,\mathcal{S}_n(\alpha, \xi)\\
&\quad + 2\Delta_n\,[1 + (-1)^n\mathrm{c}\,\mathfrak{z}^2]\exp[i\widetilde{\lambda}\,\mathrm{Im}(\alpha)]\,\mathcal{S}_n(\alpha_-, \xi)), \quad \alpha_\pm = \alpha \pm \widetilde{\lambda}.
\end{aligned} \tag{3.6}$$

For an arbitrary spin s the present approximation of the evolving bipartite state $|\psi_{_s}(t)\rangle$ produces the pure state density matrix as follows:

$$\rho^{(s)}(t) = |\psi_{_s}(t)\rangle\langle\psi_{_s}(t)|. \tag{3.7}$$

Partial tracing on the oscillator degrees of freedom contained in the density matrix (3.7) for $s = 1$ case yields the corresponding reduced qudit density matrix $\rho^{(1)}_{\mathcal{Q}}(t) = \mathrm{Tr}_{\mathcal{O}}(\rho^{(1)}(t))$:

$$\rho^{(1)}_{\mathcal{Q}}(t) = \sum_{n,\tilde{n}=0}^{\infty} \begin{pmatrix} \mathcal{B}^{(1)}_{+,n}(t)\mathcal{B}^{(1)}_{+,\tilde{n}}(t)^*\,\delta_{n\tilde{n}} & \mathcal{B}^{(1)}_{+,n}(t)\mathcal{B}^{(1)}_{0,\tilde{n}}(t)^*\,\mathcal{G}_{\tilde{n}n}(-\widetilde{\lambda}) & \mathcal{B}^{(1)}_{+,n}(t)\mathcal{B}^{(1)}_{-,\tilde{n}}(t)^*\,\mathcal{G}_{\tilde{n}n}(-2\widetilde{\lambda}) \\ \mathcal{B}^{(1)}_{0,n}(t)\mathcal{B}^{(1)}_{+,\tilde{n}}(t)^*\,\mathcal{G}_{\tilde{n}n}(\widetilde{\lambda}) & \mathcal{B}^{(1)}_{0,n}(t)\mathcal{B}^{(1)}_{0,\tilde{n}}(t)^*\,\delta_{n\tilde{n}} & \mathcal{B}^{(1)}_{0,n}(t)\mathcal{B}^{(1)}_{-,\tilde{n}}(t)^*\,\mathcal{G}_{\tilde{n}n}(-\widetilde{\lambda}) \\ \mathcal{B}^{(1)}_{-,n}(t)\mathcal{B}^{(1)}_{+,\tilde{n}}(t)^*\,\mathcal{G}_{\tilde{n}n}(2\widetilde{\lambda}) & \mathcal{B}^{(1)}_{-,n}(t)\mathcal{B}^{(1)}_{0,\tilde{n}}(t)^*\,\mathcal{G}_{\tilde{n}n}(\widetilde{\lambda}) & \mathcal{B}^{(1)}_{-,n}(t)\mathcal{B}^{(1)}_{-,\tilde{n}}(t)^*\,\delta_{n\tilde{n}} \end{pmatrix}, \tag{3.8}$$

where the elements are expressed via the sum of the factorized time-dependent components as

$$\mathcal{B}^{(1)}_{0,n}(t) = \frac{1}{\sqrt{\mathcal{N}^{(1)}_{+,n}}}\,(\widetilde{\lambda}^2+\delta_n)\,\exp\big(-iE^{(1)}_{+,n}t\big)\,\mathcal{A}^{(1)}_{+,n} + \frac{1}{\sqrt{\mathcal{N}^{(1)}_{-,n}}}\,(\widetilde{\lambda}^2-\delta_n)\,\exp\big(-iE^{(1)}_{-,n}t\big)\,\mathcal{A}^{(1)}_{-,n},$$

$$\mathcal{B}^{(1)}_{\pm,n}(t) = \pm\frac{1}{\sqrt{2}}\,\exp\big(-iE^{(1)}_{0,n}t\big)\,\mathcal{A}^{(1)}_{0,n} + 2\,\frac{\Delta_n}{\sqrt{\mathcal{N}^{(1)}_{+,n}}}\,\exp\big(-iE^{(1)}_{+,n}t\big)\,\mathcal{A}^{(1)}_{+,n} + 2\,\frac{\Delta_n}{\sqrt{\mathcal{N}^{(1)}_{-,n}}}\,\exp\big(-iE^{(1)}_{-,n}t\big)\,\mathcal{A}^{(1)}_{-,n}. \tag{3.9}$$

The off-diagonal elements of the density operator (3.8) carry the correlation functions of the oscillator number states:

$$\mathcal{G}_{mn}(\mathcal{X}) \equiv \langle m|\mathrm{D}(\mathcal{X})|n\rangle = \begin{cases} \exp\big(-\frac{|\mathcal{X}|^2}{2}\big)\mathcal{X}^{m-n}\sqrt{\frac{n!}{m!}}\;L_n^{m-n}(|\mathcal{X}|^2) & \forall\; m\geqslant n,\\ \exp\big(-\frac{|\mathcal{X}|^2}{2}\big)(-\mathcal{X}^*)^{n-m}\sqrt{\frac{m!}{n!}}\;L_m^{n-m}(|\mathcal{X}|^2) & \forall\; m<n. \end{cases} \tag{3.10}$$

The qudit density matrix (3.8) maintains the required normalization restriction: $\mathrm{Tr}\rho^{(1)}_{\mathcal{Q}}=1$. The oscillator-reduced density matrix for the $s=1$ example may also be extracted by partial tracing of the spin variable in the bipartite pure state. We do not reproduce the result here.

IV. PHASE-SPACE REPRESENTATION OF THE EVOLVING HYBRID SYSTEM

To express the phase-space quasiprobability densities for the spin variable the author of Ref. [48] introduced the spherical tensor operator

$$T_{kq} = \sum_{m,m'}(-1)^{s-m}\,\sqrt{2\,k\,+1}\begin{pmatrix} s & k & s\\ -m & q & m'\end{pmatrix}|s\,m\rangle\langle\,s\,m'|,\quad T^{\dagger}_{kq} = (-1)^q\,T_{k,-q}, \tag{4.1}$$

where the indices read as $k\in(0,1,\ldots,2s)$, $q\in(-k,-k+1,\ldots,k)$. The Wigner $3j$ coefficient appearing above follows the standard definition [54]

$$\begin{pmatrix} j_1 & j_2 & j_3\\ m_1 & m_2 & m_3\end{pmatrix} = (-1)^{j_1-j_2-m_3}\,(2\,j_3\,+1)^{-\frac{1}{2}}\,\langle j_1\,m_1;\,j_2\,m_2|j_3,\,-m_3\rangle. \tag{4.2}$$

Towards constructing the phase-space distributions for the hybrid bipartite system we employ the direct product of the spherical tensor (4.1) and the unit operator acting on the oscillator Hilbert space: $\mathcal{T}_{kq}=T_{kq}\otimes\mathbb{I}_{\mathcal{O}}$. The bipartite density matrix $\rho^{(s)}(t)$ given in (3.7) may now be utilized in the manner of [48] to acquire the spherical tensor components in the compounded Hilbert space:

$$\varrho_{kq} = \mathrm{Tr}_{\mathcal{Q}}\,[\rho^{(s)}(t)\,\mathcal{T}^{\dagger}_{kq}]. \tag{4.3}$$

In (4.3) the indices referring to the oscillator variable are not explicitly notified. A partial tracing on the oscillator degree of freedom in (4.3) readily furnishes the qudit-reduced density matrix in the spherical tensor basis [48]:

$$\varrho^{\mathcal{Q}}_{kq} \equiv \mathrm{Tr}_{\mathcal{O}}[\varrho_{kq}] = (-1)^q\sum_{m,m'}(-1)^{s-m}\,\sqrt{2k+1}\begin{pmatrix} s & s & k\\ m & -m' & q\end{pmatrix}(\rho_{\mathcal{Q}})_{m'm},\quad (\rho_{\mathcal{Q}})_{m'm} = \langle s\,m'|\,\rho_{\mathcal{Q}}\,|s\,m\rangle\,. \tag{4.4}$$

For the $s=1$ case its structure is obtained via (3.8) and (4.4):

$$\begin{aligned}\varrho^{\mathcal{Q}}_{kq}(t)\big|_{s=1} = \sqrt{\frac{2k+1}{(2-k)!(3+k)!}}\sum_{n,\widetilde{n}=0}^{\infty}\Big(&\delta_{n\widetilde{n}}\delta_{q,0}\big[2\big(\mathcal{B}^{(1)}_{+,n}(t)\,\mathcal{B}^{(1)}_{+,\widetilde{n}}(t)^* + (-1)^k\mathcal{B}^{(1)}_{-,n}(t)\,\mathcal{B}^{(1)}_{-,\widetilde{n}}(t)^*\big)\\ &-(k^2+k-2)\,\mathcal{B}^{(1)}_{0,n}(t)\,\mathcal{B}^{(1)}_{0,\widetilde{n}}(t)^*\big] - \delta_{q,1}\sqrt{2\,\frac{(k+1)!}{(k-1)!}}\,\mathcal{G}_{\widetilde{n}n}(-\widetilde{\lambda})\big[\mathcal{B}^{(1)}_{+,n}(t)\,\mathcal{B}^{(1)}_{0,\widetilde{n}}(t)^*\\ &-(-1)^k\mathcal{B}^{(1)}_{0,n}(t)\,\mathcal{B}^{(1)}_{-,\widetilde{n}}(t)^*\big] + \delta_{q,-1}\sqrt{2\,\frac{(k+1)!}{(k-1)!}}\,\mathcal{G}_{\widetilde{n}n}(\widetilde{\lambda})\Big(\mathcal{B}^{(1)}_{0,n}(t)\,\mathcal{B}^{(1)}_{+,\widetilde{n}}(t)^*\\ &-(-1)^k\mathcal{B}^{(1)}_{-,n}(t)\,\mathcal{B}^{(1)}_{0,\widetilde{n}}(t)^*\Big) + \sqrt{\frac{(k+2)!}{(k-2)!}}\big(\delta_{q,-2}\,\mathcal{G}_{\widetilde{n}n}(2\widetilde{\lambda})\,\mathcal{B}^{(1)}_{-,n}(t)\,\mathcal{B}^{(1)}_{+,\widetilde{n}}(t)^*\\ &+(-1)^k\delta_{q,2}\,\mathcal{G}_{\widetilde{n}n}(-2\widetilde{\lambda})\,\mathcal{B}^{(1)}_{+,n}(t)\,\mathcal{B}^{(1)}_{-,\widetilde{n}}(t)^*\big)\Big).\end{aligned} \tag{4.5}$$

Adapting the formulation in Ref. [48] for the spin variable and the well-known description of the oscillator degree of freedom [49,50], we now propose the phase-space quasiprobability distributions of the bipartite system via the decomposition (4.3) of

the compounded density matrix. In particular, the diagonal P representation of the qudit-oscillator interacting system may be constructed as

$$\mathrm{P}(\theta,\phi;\beta,\beta^*)=\frac{\exp(|\beta|^2)}{\pi^2}\sum_{k,q}(-1)^{k-q}\,c_{kq}\left(\int\langle-\gamma|\,\varrho_{kq}\,|\gamma\rangle\exp(|\gamma|^2)\exp(\beta\,\gamma^*-\beta^*\,\gamma)\,d^2\gamma\right)Y_{kq}(\theta,\phi),\tag{4.6}$$

where the spin coefficient reads as [48] $c_{kq}=\frac{\sqrt{(2\,s-k)!\,(2\,s+k+1)!}}{\sqrt{4\,\pi}\,(2\,s)!}$. The coherent states $\{|\gamma\rangle\,,\gamma\in\mathbb{C}\}$ in the oscillator phase space facilitate, via an inverse Fourier transform [49], furnishing the diagonal $\mathrm{P}(\theta,\phi;\beta,\beta^*)$ representation for the bipartite density matrix. The spherical harmonics appearing in (4.6) follow the standard definition [54]. Maintaining its characteristics for individual phase spaces [48,55] the P representation provides a diagonal factorized coherent state description of an arbitrary bipartite qudit-oscillator density matrix:

$$\rho(t)=\int\mathrm{P}(\theta,\phi;\beta,\beta^*)\;|\theta,\phi;\beta\rangle\,\langle\theta,\phi;\beta|\;\,d\Omega\,d^2\beta,\quad d\Omega=\sin\theta\,d\theta\,d\phi.\tag{4.7}$$

The diagonal $\mathrm{P}_{\mathcal{Q}}$ representation for the spin variable [48] may be procured by integrating the bipartite quasiprobability density (4.6) on the oscillator phase space:

$$\mathrm{P}_{\mathcal{Q}}(\theta,\phi)\equiv\int\mathrm{P}(\theta,\phi;\beta,\beta^*)\,d^2\beta\;\;\Rightarrow\;\;\mathrm{P}_{\mathcal{Q}}(\theta,\phi)=\sum_{kq}(-1)^{k-q}\,c_{kq}\,\varrho^{\mathcal{Q}}_{kq}\,Y_{kq}(\theta,\phi),\quad\int\mathrm{P}_{\mathcal{Q}}(\theta,\phi)d\Omega=1.\tag{4.8}$$

Modulo our approximation, Eq. (4.8) admits explicit evaluation of the qudit $\mathrm{P}_{\mathcal{Q}}(\theta,\phi)$ representation, say for the $s=1$ and $\frac{3}{2}$ cases, via the substitution of the corresponding density matrices in the spherical tensor basis given in (4.5) and (B10), respectively. Unlike its oscillator counterpart, the spin $\mathrm{P}_{\mathcal{Q}}$ representation is nonsingular, and, therefore, may be fruitfully applied to observe the phase-space structures such as the transient spin kitten type states.

The construction of the hybrid bipartite Wigner W distribution in the product phase space may be similarly established. Maintaining the compositions of the individual phase-space Wigner functions for the spin and oscillator variables, we construct the W distribution for the interacting system as

$$\mathrm{W}(\theta,\phi;\beta,\beta^*)=\frac{1}{\pi^2}\sqrt{\frac{2s+1}{4\pi}}\sum_{kq}\left(\int\mathrm{Tr}_{\mathcal{O}}\big[\varrho_{kq}\mathrm{D}(\gamma)\big]\exp(\beta\,\gamma^*-\beta^*\,\gamma)\,d^2\gamma\right)Y_{kq}(\theta,\phi).\tag{4.9}$$

The above Wigner distribution (4.9) may be recast in the manner of [56] as an infinite alternating series sum of the diagonal matrix elements of the density operator in the displaced oscillator number state basis:

$$\mathrm{W}(\theta,\phi;\beta,\beta^*)=\frac{2}{\pi}\sqrt{\frac{2s+1}{4\pi}}\sum_{kq}\sum_{n=0}^{\infty}(-1)^n\,\langle\beta,n|\varrho_{kq}|\beta,n\rangle\,Y_{kq}(\theta,\phi),\quad|\beta,n\rangle=\mathrm{D}(\beta)\,|n\rangle\,.\tag{4.10}$$

An integration of the bipartite quasiprobability function (4.9) over the oscillator phase space generates the Wigner distribution for the spin degree of freedom [57]:

$$\mathrm{W}_{\mathcal{Q}}(\theta,\phi)\equiv\int\mathrm{W}(\theta,\phi;\beta,\beta^*)\,d^2\beta\;\;\Rightarrow\;\;\mathrm{W}_{\mathcal{Q}}(\theta,\phi)=\sqrt{\frac{2s+1}{4\pi}}\sum_{kq}\varrho^{\mathcal{Q}}_{kq}\,Y_{kq}(\theta,\phi),\quad\int\mathrm{W}_{\mathcal{Q}}(\theta,\phi)\,d\Omega=1.\tag{4.11}$$

Continuing our description of the bipartite quasiprobability functions on the joint phase space we now constitute the positive-semidefinite Husimi Q function for the combined spin-oscillator system via the spherical tensor decomposition (4.3) of the compounded density matrix:

$$\mathrm{Q}(\theta,\phi;\beta,\beta^*)=\frac{2\,s+1}{4\,\pi^2}\sum_{kq}(-1)^{k-q}\,(c_{kq})^{-1}\;\langle\beta|\,\varrho_{kq}\,|\beta\rangle\;Y_{kq}(\theta,\phi).\tag{4.12}$$

The Q function for the spin degree of freedom [48] is recovered from the bipartite construction (4.12) by an integration over the oscillator phase space:

$$\mathrm{Q}_{\mathcal{Q}}(\theta,\phi)\equiv\int\mathrm{Q}(\theta,\phi;\beta,\beta^*)\,d^2\beta\Rightarrow\mathrm{Q}_{\mathcal{Q}}(\theta,\phi)=\frac{2\,s+1}{4\,\pi}\sum_{kq}(-1)^{k-q}\,(c_{kq})^{-1}\varrho^{\mathcal{Q}}_{kq}\,Y_{kq}(\theta,\phi),\;\int\mathrm{Q}_{\mathcal{Q}}(\theta,\phi)d\Omega=1.\tag{4.13}$$

We also briefly summarize the recipe for constructing the normalized oscillator quasiprobability distributions starting from the bipartite phase-space densities. Integration of the bipartite distributions over the qudit spherical phase space leads to the

corresponding oscillator quasiprobabilities [50] listed below:

$$\int \mathrm{P}(\theta,\phi;\beta,\beta^*)\,d\Omega \equiv \mathrm{P}_{\mathcal{O}}(\beta,\beta^*) = \frac{\exp(|\beta|^2)}{\pi^2}\int \langle -\gamma|\,\rho_{\mathcal{O}}\,|\gamma\rangle\,\exp(|\gamma|^2)\exp(\beta\,\gamma^* - \beta^*\,\gamma)\,d^2\gamma, \tag{4.14}$$

$$\int \mathrm{W}(\theta,\phi;\beta,\beta^*)d\Omega \equiv \mathrm{W}_{\mathcal{O}}(\beta,\beta^*) = \frac{1}{\pi^2}\int \mathrm{Tr}_{\mathcal{O}}\big[\rho_{\mathcal{O}}\mathrm{D}(\gamma)\big]\exp(\beta\,\gamma^* - \beta^*\,\gamma)\,d^2\gamma, \tag{4.15}$$

$$\int \mathrm{Q}(\theta,\phi;\beta,\beta^*)d\Omega \equiv \mathrm{Q}_{\mathcal{O}}(\beta,\beta^*) = \frac{1}{\pi}\,\langle\beta|\rho_{\mathcal{O}}|\beta\rangle\,. \tag{4.16}$$

A. Explicit structures of the hybrid phase-space distributions for the $s = 1$ case

The bipartite P representation (4.6) may be explicitly determined by employing the composite density matrix elements (4.3). The $s = 1$ example reads as

$$\begin{aligned}\mathrm{P}^{(1)}(\theta,\phi;\beta,\beta^*) = \frac{1}{16\pi}\sum_{n,\widetilde{n}=0}^{\infty}\Big\{&3(3-4\cos\theta+5\cos 2\theta)\mathcal{B}^{(1)}_{+,n}(t)\mathcal{B}^{(1)}_{+,\widetilde{n}}(t)^*\Lambda_1^{n,\widetilde{n}} - 6(1+5\cos 2\theta)\\ &\times\mathcal{B}^{(1)}_{0,n}(t)\mathcal{B}^{(1)}_{0,\widetilde{n}}(t)^*\Lambda_0^{n,\widetilde{n}} + 3(3+4\cos\theta+5\cos 2\theta)\,\mathcal{B}^{(1)}_{-,n}(t)\mathcal{B}^{(1)}_{-,\widetilde{n}}(t)^*\Lambda_{-1}^{n,\widetilde{n}}\\ &+\sum_{k=0}^{\infty}\big[12\sqrt{2}\sin\theta(1-5\cos\theta)\,\mathrm{Re}\big(\exp(i\phi)\mathcal{B}^{(1)}_{+,n}(t)\mathcal{B}^{(1)}_{0,\widetilde{n}}(t)^*\,\mathcal{G}_{kn}(-\widetilde{\lambda})\Lambda_0^{k,\widetilde{n}}\big)\\ &+12\sqrt{2}\sin\theta(1+5\cos\theta)\,\mathrm{Re}\big(\exp(-i\phi)\,\mathcal{B}^{(1)}_{-,n}(t)\mathcal{B}^{(1)}_{0,\widetilde{n}}(t)^*\,\mathcal{G}_{kn}(\widetilde{\lambda})\Lambda_0^{k,\widetilde{n}}\big)\big]\\ &+\sum_{k,\ell=0}^{\infty}60\sin^2\theta\,\mathrm{Re}\big(\exp(2i\phi)\mathcal{B}^{(1)}_{+,n}(t)\mathcal{B}^{(1)}_{-,\widetilde{n}}(t)^*\mathcal{G}_{kn}(-\widetilde{\lambda})\,\mathcal{G}_{\widetilde{n}\ell}(-\widetilde{\lambda})\Lambda_0^{k,\ell}\big)\Big\},\end{aligned} \tag{4.17}$$

where the weighted distribution has the form $\Lambda_m^{n,\widetilde{n}} = \frac{1}{\sqrt{n!\widetilde{n}!}}\exp(|\beta_m|^2)(-\frac{\partial}{\partial\beta_m})^n(-\frac{\partial}{\partial\beta_m^*})^{\widetilde{n}}\delta^{(2)}(\beta_m)$, and the spin-dependent displaced coordinate is given by $\beta_m = \beta + m\widetilde{\lambda}$. The oscillator phase-space integral of the composite quasiprobability density (4.17) provides, in the manner of (4.8), the qudit $s = 1$ diagonal $\mathrm{P}_{\mathcal{Q}}$ representation

$$\begin{aligned}\mathrm{P}^{(1)}_{\mathcal{Q}}(\theta,\phi) = \frac{1}{16\pi}\sum_{n,\widetilde{n}=0}^{\infty}\big\{&3\,(3-4\cos\theta+5\cos 2\theta)\mathcal{B}^{(1)}_{+,n}(t)\mathcal{B}^{(1)}_{+,\widetilde{n}}(t)^*\,\delta_{n\widetilde{n}} - 6\,(1+5\cos 2\theta)\,\mathcal{B}^{(1)}_{0,n}(t)\mathcal{B}^{(1)}_{0,\widetilde{n}}(t)^*\,\delta_{n\widetilde{n}}\\ &+3\,(3+4\cos\theta+5\cos 2\theta)\mathcal{B}^{(1)}_{-,n}(t)\mathcal{B}^{(1)}_{-,\widetilde{n}}(t)^*\,\delta_{n\widetilde{n}} + 12\,\sqrt{2}\sin\theta(1-5\cos\theta)\mathrm{Re}\big(\exp(i\phi)\\ &\times\mathcal{B}^{(1)}_{+,n}(t)\mathcal{B}^{(1)}_{0,\widetilde{n}}(t)^*\mathcal{G}_{\widetilde{n}n}(-\widetilde{\lambda})\big) + 12\sqrt{2}\sin\theta(1+5\cos\theta)\mathrm{Re}\big(\exp(-i\phi)\mathcal{B}^{(1)}_{-,n}(t)\mathcal{B}^{(1)}_{0,\widetilde{n}}(t)^*\mathcal{G}_{\widetilde{n}n}(\widetilde{\lambda})\big)\\ &+60\,\sin^2\theta\,\mathrm{Re}\big(\exp(2i\phi)\mathcal{B}^{(1)}_{+,n}(t)\mathcal{B}^{(1)}_{-,\widetilde{n}}(t)^*\mathcal{G}_{\widetilde{n}n}(-2\widetilde{\lambda})\big)\big\}.\end{aligned} \tag{4.18}$$

Alternately, (4.18) may be directly computed via the corresponding spin density matrix (4.5) in the spherical tensor basis and the construction [48] of the $\mathrm{P}_{\mathcal{Q}}(\theta,\phi)$ representation appearing at the first equality in (4.8). This provides a consistency check on the structure of the hybrid P representation (4.6). Similarly, the composition (4.10) of the bipartite Wigner W distribution provides its explicit evaluation for the $s = 1$ case:

$$\begin{aligned}\mathrm{W}^{(1)}(\theta,\phi;\beta,\beta^*) = \frac{1}{16\pi^2}\sum_{n,\widetilde{n}=0}^{\infty}\big((8+\sqrt{10}+12\sqrt{2}\cos\theta+3\sqrt{10}\cos 2\theta)\mathcal{H}^{n,\widetilde{n}}_{1,1}(\beta,\beta^*)\mathcal{B}^{(1)}_{+,n}(t)\mathcal{B}^{(1)}_{+,\widetilde{n}}(t)^*\\ +\big(8+4\sqrt{10}-12\sqrt{10}\cos^2\theta\big)\mathcal{H}^{n,\widetilde{n}}_{0,0}(\beta,\beta^*)\mathcal{B}^{(1)}_{0,n}(t)\mathcal{B}^{(1)}_{0,\widetilde{n}}(t)^* + \big(8+\sqrt{10}-12\sqrt{2}\cos\theta\\ +3\sqrt{10}\cos 2\theta\big)\mathcal{H}^{n,\widetilde{n}}_{-1,-1}(\beta,\beta^*)\mathcal{B}^{(1)}_{-,n}(t)\mathcal{B}^{(1)}_{-,\widetilde{n}}(t)^* + 24(1+\sqrt{5}\cos\theta)\sin\theta\\ \times\mathrm{Re}\big\{\mathcal{H}^{n,\widetilde{n}}_{1,0}(\beta,\beta^*)\exp[i(\phi+\widetilde{\lambda}\mathrm{Im}(\beta))]\mathcal{B}^{(1)}_{+,n}(t)\mathcal{B}^{(1)}_{0,\widetilde{n}}(t)^*\big\} + 24(1-\sqrt{5}\cos\theta)\sin\theta\\ \times\mathrm{Re}\big\{\mathcal{H}^{n,\widetilde{n}}_{-1,0}(\beta,\beta^*)\exp\big[i\big(\phi+\widetilde{\lambda}\mathrm{Im}(\beta)\big)\big]\mathcal{B}^{(1)}_{-,n}(t)\mathcal{B}^{(1)}_{0,\widetilde{n}}(t)^*\big\} + 12\sqrt{10}\,\sin^2\theta\\ \times\mathrm{Re}\big\{\mathcal{H}^{n,\widetilde{n}}_{1,-1}(\beta,\beta^*)\exp[2i(\phi+\widetilde{\lambda}\mathrm{Im}(\beta))]\mathcal{B}^{(1)}_{+,n}(t)\mathcal{B}^{(1)}_{-,\widetilde{n}}(t)^*\big\}\big),\end{aligned} \tag{4.19}$$

where the complex Gaussian structure stands as

$$\mathcal{H}^{n,\widetilde{n}}_{k,\ell}(\beta,\beta^*)=\frac{1}{\sqrt{n!\widetilde{n}!}}(\beta_k^*+\beta_\ell^*)^n(\beta_k+\beta_\ell)^{\widetilde{n}}\exp\left(-\frac{1}{2}(|\beta_k|^2+|\beta_\ell|^2)-\beta_k\beta_\ell^*\right){}_2F_0\left(-n,-\widetilde{n};\_;-\frac{1}{|\beta_k+\beta_\ell|^2}\right)$$

and the hypergeometric sum is given by [58] ${}_2F_0(\mathsf{x},\mathsf{y};\_;\tau)=\sum_{k=0}^{\infty}(\mathsf{x})_k(\mathsf{y})_k\,\frac{\tau^k}{k!}$, $(\mathsf{x})_k=\prod_{\ell=0}^{k-1}(\mathsf{x}+\ell)$. Choosing negative integers as numerator coefficients the function ${}_2F_0$ may be expressed [59] via the Charlier polynomial $\mathrm{c}_k(\ell;\tau)={}_2F_0(-k,-\ell;\_;-\frac{1}{\tau})\ \forall\ \tau>0$. To derive the bipartite W distribution (4.19) we utilize an identity [59] that readily follows from the bilinear generating function of the Charlier polynomials:

$$\sum_{k=0}^{\infty}\frac{(-1)^k\tau^k}{k!}\,{}_2F_0\Big(-n,-k;\_;-\frac{1}{\mathsf{x}}\Big)\,{}_2F_0\Big(-k,-m;\_;-\frac{1}{\mathsf{y}}\Big)=\Big(1+\frac{\tau}{\mathsf{x}}\Big)^n\Big(1+\frac{\tau}{\mathsf{y}}\Big)^m\exp(-\tau)$$
$$\times{}_2F_0\Big(-n,-m;\_;-\frac{\tau}{(\mathsf{x}+\tau)(\mathsf{y}+\tau)}\Big).\tag{4.20}$$

A reduction of the phase space via the integration over the complex plane given in (4.11) now procures the qudit $\mathrm{W}_{\mathcal{Q}}$ distribution concretely for the $s=1$ case:

$$\begin{aligned}\mathrm{W}^{(1)}_{\mathcal{Q}}(\theta,\phi)=\frac{1}{32\pi}\sum_{n,\widetilde{n}=0}^{\infty}\big\{&(8+\sqrt{10}+12\sqrt{2}\cos\theta+3\sqrt{10}\cos2\theta)\mathcal{B}^{(1)}_{+,n}(t)\mathcal{B}^{(1)}_{+,\widetilde{n}}(t)^*\,\delta_{n\widetilde{n}}+(8+4\sqrt{10}\\&-12\sqrt{10}\cos^2\theta)\mathcal{B}^{(1)}_{0,n}(t)\mathcal{B}^{(1)}_{0,\widetilde{n}}(t)^*\,\delta_{n\widetilde{n}}+(8+\sqrt{10}-12\sqrt{2}\cos\theta+3\sqrt{10}\cos2\theta)\\&\times\mathcal{B}^{(1)}_{-,n}(t)\mathcal{B}^{(1)}_{-,\widetilde{n}}(t)^*\,\delta_{n\widetilde{n}}+24(1+\sqrt{5}\cos\theta)\sin\theta\ \mathrm{Re}\big(\exp(i\phi)\ \mathcal{B}^{(1)}_{+,n}(t)\mathcal{B}^{(1)}_{0,\widetilde{n}}(t)^*\mathcal{G}_{\widetilde{n}n}(-\widetilde{\lambda})\big)\\&+24(1-\sqrt{5}\cos\theta)\sin\theta\ \mathrm{Re}\big(\exp(-i\phi)\ \mathcal{B}^{(1)}_{-,n}(t)\mathcal{B}^{(1)}_{0,\widetilde{n}}(t)^*\mathcal{G}_{\widetilde{n}n}(\widetilde{\lambda})\big)+12\sqrt{10}\ \sin^2\theta\\&\times\mathrm{Re}\big(\exp(2i\phi)\ \mathcal{B}^{(1)}_{+,n}(t)\mathcal{B}^{(1)}_{-,\widetilde{n}}(t)^*\mathcal{G}_{\widetilde{n}n}(-2\widetilde{\lambda})\big)\big\}.\end{aligned}\tag{4.21}$$

The above expression may also be directly obtained by applying our evaluation of the spin density matrix (4.5) in a spherical basis, and utilizing the construction [48] of the $\mathrm{W}_{\mathcal{Q}}(\theta,\phi)$ representation realized in (4.11). This implements a consistency check on the validity of the hybrid W representation (4.9) advanced here. We also proceed with a similar demonstration of the bipartite Q function given in (4.12). The compounded Q function for the qudit-oscillator system may be composed by employing the corresponding hybrid density matrix (4.3). The $s=1$ example is quoted below:

$$\begin{aligned}\mathrm{Q}^{(1)}(\theta,\phi;\beta,\beta^*)=\frac{3}{4\pi^2}\sum_{n,\widetilde{n}=0}^{\infty}\Bigg(&\sin^4\Big(\frac{\theta}{2}\Big)\mathcal{Y}^{n,\widetilde{n}}_{1,1}(\beta,\beta^*)\mathcal{B}^{(1)}_{+,n}(t)\mathcal{B}^{(1)}_{+,\widetilde{n}}(t)^*+\frac{\sin^2\theta}{2}\mathcal{Y}^{n,\widetilde{n}}_{0,0}(\beta,\beta^*)\mathcal{B}^{(1)}_{0,n}(t)\mathcal{B}^{(1)}_{0,\widetilde{n}}(t)^*\\&+\cos^4\Big(\frac{\theta}{2}\Big)\mathcal{Y}^{n,\widetilde{n}}_{-1,-1}(\beta,\beta^*)\mathcal{B}^{(1)}_{-,n}(t)\mathcal{B}^{(1)}_{-,\widetilde{n}}(t)^*+\sqrt{2}\sin\theta\sin^2\Big(\frac{\theta}{2}\Big)\mathrm{Re}\big\{\mathcal{Y}^{n,\widetilde{n}}_{1,0}(\beta,\beta^*)\\&\times\exp[i(\phi+\widetilde{\lambda}\mathrm{Im}(\beta))]\mathcal{B}^{(1)}_{+,n}(t)\mathcal{B}^{(1)}_{0,\widetilde{n}}(t)^*\big\}+\sqrt{2}\sin\theta\cos^2\Big(\frac{\theta}{2}\Big)\mathrm{Re}\big\{\mathcal{Y}^{n,\widetilde{n}}_{-1,0}(\beta,\beta^*)\\&\times\exp[-i(\phi+\widetilde{\lambda}\mathrm{Im}(\beta))]\mathcal{B}^{(1)}_{-,n}(t)\mathcal{B}^{(1)}_{0,\widetilde{n}}(t)^*\big\}+\frac{\sin^2\theta}{2}\mathrm{Re}\big\{\mathcal{Y}^{n,\widetilde{n}}_{1,-1}(\beta,\beta^*)\\&\times\exp[2i(\phi+\widetilde{\lambda}\mathrm{Im}(\beta))]\mathcal{B}^{(1)}_{+,n}(t)\mathcal{B}^{(1)}_{-,\widetilde{n}}(t)^*\big\}\Bigg).\end{aligned}\tag{4.22}$$

In the expression (4.22) we have employed the notation $\mathcal{Y}^{n,\widetilde{n}}_{k,\ell}(\beta,\beta^*)=\frac{1}{\sqrt{n!\widetilde{n}!}}\beta_k^{*n}\beta_\ell^{\widetilde{n}}\exp[-\frac{1}{2}(|\beta_k|^2+|\beta_\ell|^2)]$. A further integration on the oscillator variables in the manner of (4.13) now generates the $s=1$ qudit $\mathrm{Q}^{(1)}_{\mathcal{Q}}$ function that may alternately be established starting from the spin density matrix (4.5) in the spherical basis set and implementing the construction given in [48]:

$$\begin{aligned}\mathrm{Q}^{(1)}_{\mathcal{Q}}(\theta,\phi)=\frac{3}{4\pi}\sum_{n,\widetilde{n}=0}^{\infty}\Bigg\{&\sin^4\Big(\frac{\theta}{2}\Big)\mathcal{B}^{(1)}_{+,n}(t)\mathcal{B}^{(1)}_{+,\widetilde{n}}(t)^*\delta_{n\widetilde{n}}+\frac{1}{2}\sin^2\theta\ \mathcal{B}^{(1)}_{0,n}(t)\mathcal{B}^{(1)}_{0,\widetilde{n}}(t)^*\delta_{n\widetilde{n}}\\&+\cos^4\Big(\frac{\theta}{2}\Big)\mathcal{B}^{(1)}_{-,n}(t)\mathcal{B}^{(1)}_{-,\widetilde{n}}(t)^*\delta_{n\widetilde{n}}+\sqrt{2}\sin\theta\sin^2\Big(\frac{\theta}{2}\Big)\mathrm{Re}\big[\exp(i\phi)\mathcal{B}^{(1)}_{+,n}(t)\mathcal{B}^{(1)}_{0,\widetilde{n}}(t)^*\mathcal{G}_{\widetilde{n}n}(-\widetilde{\lambda})\big]\\&+\sqrt{2}\sin\theta\cos^2\Big(\frac{\theta}{2}\Big)\mathrm{Re}\big[\exp(-i\phi)\mathcal{B}^{(1)}_{-,n}(t)\mathcal{B}^{(1)}_{0,\widetilde{n}}(t)^*\mathcal{G}_{\widetilde{n}n}(\widetilde{\lambda})\big]+\frac{\sin^2\theta}{2}\mathrm{Re}\big[\exp(2i\phi)\mathcal{B}^{(1)}_{+,n}(t)\mathcal{B}^{(1)}_{-,\widetilde{n}}(t)^*\mathcal{G}_{\widetilde{n}n}(-2\widetilde{\lambda})\big]\Bigg\}.\end{aligned}\tag{4.23}$$

The preceding discussion allows us to view the hybrid bipartite phase-space quasiprobability distribution as the underlying structure that produces the appropriate qudit phase-space function after a suitable dimensional reduction.

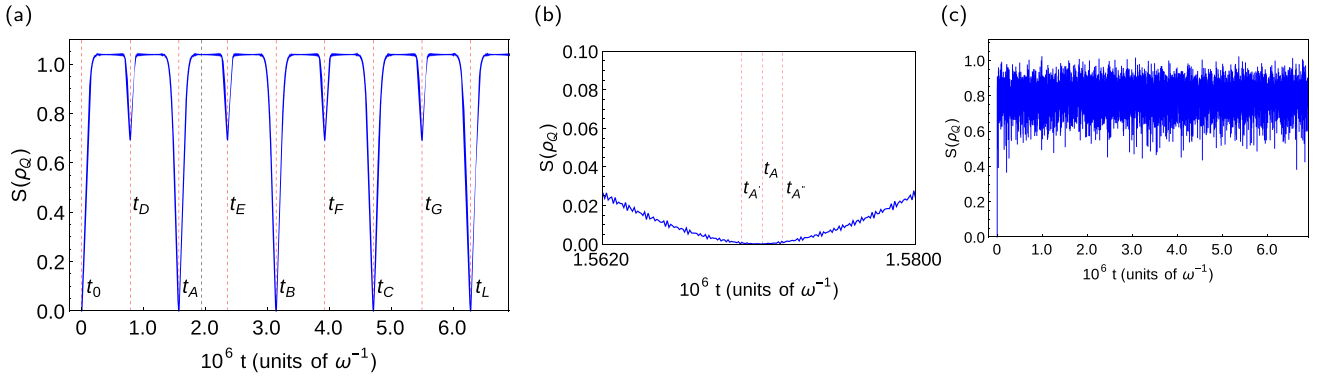

FIG. 2. For the factorized initial state (3.1) with c = 0 the time evolution of the entropy for the $s = 1$ case is studied. (a) For the strong coupling regime ($\widetilde{\lambda} = 0.005$) the chosen parametric values are as follows: $\Delta = 0.16$, $\mathfrak{z} = 0.0200$, $\alpha = 3$, $r = 0.2$. To explore the near recurrence of the initial state during the evolution the Hilbert-Schmidt distances between the initial state at $t_0 = 0$ and the states at $t_A = 1.571\,175 \times 10^6$, $t_B = 3.141\,990 \times 10^6$, $t_C = 4.712\,833 \times 10^6$, $t_L = 6.284\,030 \times 10^6$ are computed as follows: $d_{HS}|_{t_A} = 0.900\,173$, $d_{HS}|_{t_B} = 1.083\,885$, $d_{HS}|_{t_C} = 1.318\,340$, $d_{HS}|_{t_L} = 0.007\,481$. It is evident that the system achieves near reproduction of its initial state at $t_L \equiv T_{rev}$. Here and elsewhere, all times are specified in the scale ω^{-1}, and for all numerical work we use the unit $\omega = 1$. The quasiperiod (5.2) of the time evolution of the entropy for the present set of parameters equals $1.570\,816 \times 10^6$, which is nearly identical to t_A. The full revival time (5.4) now corresponds to n = 4. Locally minimum, but considerably large value of entropy is realized at time, say, $t_D = 0.785\,496 \times 10^6$. The spin states at (t_D, t_A, t_B, t_C) are studied in Fig. 3. (b) The nearly pure spin cat type states appearing at the local minima of the entropy live for moderately long intervals around the exact minima. For instance, the generalized spin cat state realized at the nearly zero-entropy configuration at t_A [Fig. 3(b)] lives for an extended period ranging between $t_{A'} = 1.569\,996 \times 10^6$ and $t_{A''} = 1.572\,354 \times 10^6$. (c) For the ultrastrong coupling regime we chose $\widetilde{\lambda} = 0.2$ while all other parameters remain identical to those in diagram (a). It is marked by loss of quasiperiodicity, and an onset of a stabilized value of entropy that experiences stochastic fluctuations.

V. MULTIPLE TIMESCALES IN THE EVOLUTION OF ENTROPY

To explore the emergence of transitory spin kitten type states and other localized configurations during the evolution generated by the bipartite Hamiltonian (2.1) at moderately strong coupling $\widetilde{\lambda} \sim O(10^{-2})$ we study the qudit entropy given by

$$S(\rho_{\mathcal{Q}}) = -\mathrm{Tr}[\rho_{\mathcal{Q}} \ln \rho_{\mathcal{Q}}], \tag{5.1}$$

where we have omitted explicit reference to the spin quantum number s. As our bipartite system inhabits a pure state, the entropies of two individual subsystems are equal [60]. It may be viewed as the entanglement entropy of the hybrid composite system. The characteristic timescale that governs the appearance of these kitten type states may be understood as follows. The terms emerging in the expansion of the Laguerre polynomials present in the off-diagonal elements of the Hamiltonian for the spin $s = 1, \frac{3}{2}$ cases given in Eqs. (2.5) and (B1), respectively, engender specific timescales inherent to the process. In the analysis presented here we explore the first nontrivial dimensionless timescale $\omega t_{long} \sim O\{[\frac{\Delta}{\omega} \exp(-\frac{\widetilde{\lambda}^2}{2})\widetilde{\lambda}^2]^{-1}\}$ that originates as a consequence of the linear term appearing in the Laguerre polynomial. For the set of parameters considered here, the above timescale is given by $\omega t_{long} \sim O(10^6)$. It is interesting to note that this scale triggering the generation of nontrivial spin states *does not* depend on the value of spin s. It may have a practical consequence that we will later comment upon. To proceed, we consider the entropy (5.1) for the spin $s = 1, \frac{3}{2}$ cases in Figs. 2(a) and 4(a), respectively. One general feature evident in these two diagrams is the existence of a quasiperiodicity of the system that implements the entropy reducing to approximately zero value repeatedly. This, in turn, imparts a near factorizability to the bipartite composite state. Following previous arguments this quasiperiod may be quantified as

$$\omega \mathrm{T}|_{\mathrm{quasiperiod}} = 2\pi \left\{ \left[\frac{\Delta}{\omega} \exp\left(-\frac{\widetilde{\lambda}^2}{2} \right) \widetilde{\lambda}^2 \right]^{-1} \right\}. \tag{5.2}$$

Our later discussions in the context of Figs. 2 and 4 regarding the evolution of specific states will support the accuracy

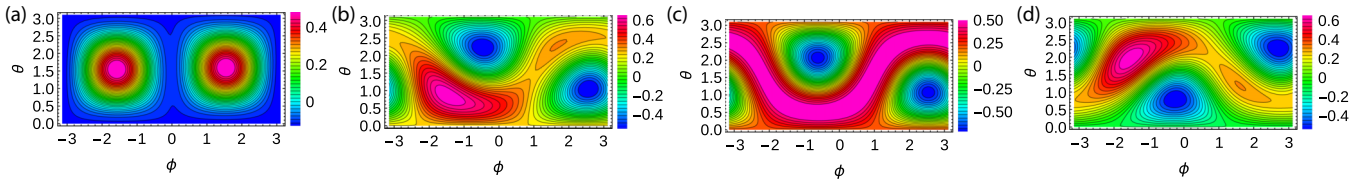

FIG. 3. We display the construction of the diagonal $P_{\mathcal{Q}}(\theta, \phi)$ representation for the $s = 1$ example studied in Fig. 2(a). The diagrams (a)–(d) refer, successively, to the times t_D, t_A, t_B, t_C therein. The bilocalized spin state, evident in the illustration (a) above, is realized at t_D when the nonzero locally minimum entropy induces a mixed-state density matrix. The spin cat type states depicted in (b), (c), and (d) arise at times (t_A, t_B, t_C), consecutively. They refer to nearly pure state density matrices reflecting superposition of spin coherent states (Table III).

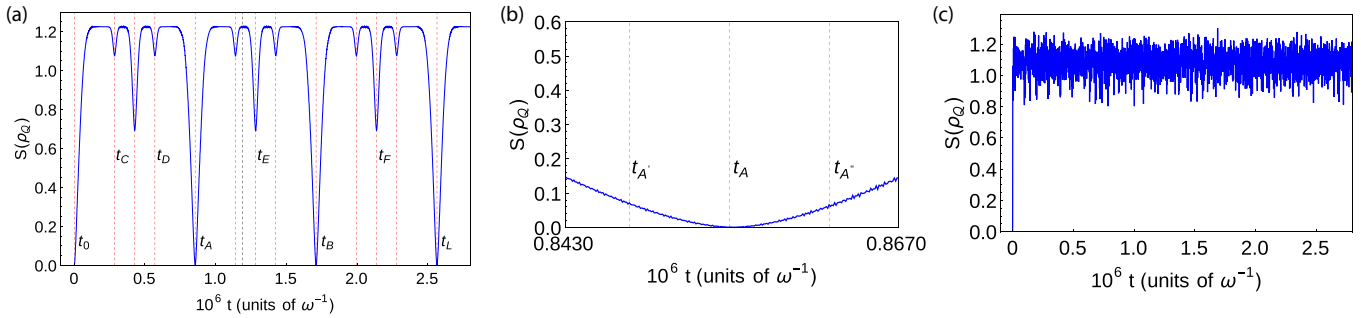

FIG. 4. The quasiperiodic evolution of the entropy for the $s = \frac{3}{2}$ case is produced for the factorized initial state (3.1) with c = 0. (a) Here the chosen parameters are $\Delta = 0.15$, $\mathfrak{z} = 0.1051$, $\alpha = 3$, $r = 0.2$, and the coupling strength equals $\widetilde{\lambda} = 0.007$. The Hilbert-Schmidt distance is studied to infer the closeness of the evolving state with its initial ($t_0 = 0$) counterpart. At times $t_A = 0.854\,819 \times 10^6$, $t_B = 1.710\,040 \times 10^6$, $t_L = 2.564\,985 \times 10^6$ the state achieves near-null entropy configurations. The Hilbert-Schmidt distances between the initial state and the qudit states at these times $d_{HS}|_{t_A} = 0.917\,149$, $d_{HS}|_{t_B} = 0.924\,257$, $d_{HS}|_{t_L} = 0.019\,044$ suggest near duplication of the initial state at time $t_L \equiv T_{rev}$. For the current set of parameters the quasiperiod (5.2) of the near-null value of the entropy stands as $0.854\,876 \times 10^6$, which closely equals t_A. The corresponding full revival time (5.4) is given by $\mathfrak{n} = 3$. The observed transitory spin kitten type states occurring at times (t_A, t_B) are specified in Figs. 5(b) and 5(c). The 3-localized spin state [Fig. 5(a)] observed, say, at time $t_D = 0.570\,000 \times 10^6$ corresponds to locally minimum but markedly large entropy [$S(\rho_Q) \lesssim O(\ln 4)$]. (b) The three-spin kitten type state formed, for instance, at time t_A lives for an elongated time period ranging between $t_{A'} = 0.847\,608 \times 10^6$ and $t_{A''} = 0.862\,007 \times 10^6$. (c) For the ultrastrong coupling regime $\widetilde{\lambda} = 0.2$ [all other parameters retain their values considered in (a)] the quasiperiodicity of the evolving state is lost. Random fluctuations occur around a steady state of entropy.

of this description. Towards checking the true periodicity of the system we evaluate the Hilbert-Schmidt distance [61] between the initial qudit state and the evolving state under investigation. Between any two arbitrary density matrices $((\rho_Q)_1, (\rho_Q)_2)$ the Hilbert-Schmidt distance is defined as follows:

$$[d_{HS}((\rho_Q)_1, (\rho_Q)_2)]^2 \equiv \mathrm{Tr}[[(\rho_Q)_1 - (\rho_Q)_2]^2] = \frac{4\pi}{2s+1} \int [(\mathrm{W}_Q(\theta,\phi))_1 - (\mathrm{W}_Q(\theta,\phi))_2]^2 d\Omega. \quad (5.3)$$

The equality in (5.3) follows from the definition (4.11). It succinctly expresses the metric $d_{HS}((\rho_Q)_1, (\rho_Q)_2)$ on the Hilbert space via the corresponding spin Wigner $\mathrm{W}_Q(\theta,\phi)$ distributions. The distance measures between the initial state and various states in question are quoted in Figs. 2(a) and 4(a). In these illustrations we notice that the system returns, in a timescale, say T_{rev}, close to its initial state after an integral number of its arrivals to the approximately zero-entropy configurations. Roughly speaking, we obtain

$$T_{rev} \approx \mathfrak{n} T|_{\text{quasiperiod}}, \quad (5.4)$$

where $\mathfrak{n}$ is a small positive integer. The near reproduction of the original state in the phase space may be considered as a spin analog of the quantum revival of a wave packet [62]. We will later observe (Sec. VI A) that the approximately zero-entropy configurations [$S(\rho_Q) \ll 1$], which are significantly distinct from the initial state as measured by the metric (5.3) [$d_{HS}(\rho_Q(t_0), \rho_Q(t)) \sim O(1)$], display characteristic properties of generalized spin kitten states. Being endowed with near-null values of entropy, these qudit states are almost pure in nature. Another feature noticed in Figs. 2(a) and 4(a) is the almost periodic manifestation of the locally minimum, but, nonetheless, appreciably large entropy configurations $S(\rho_Q) \lesssim O[\ln(2s+1)]$. The eigenvalues of the spin density matrix ρ_Q at these times are dominated by several large entries. This suggests that mixed qudit states at considerable distances from nearly pure ones are realized at these instants. The formation of these entropy minima states has close correspondence with the fractional revival of the wave packets [62]. Akin to the system of wave packets, the present bipartite system also maintains the time of manifestation of the quantum fractional revivals as $\frac{k}{\ell} T_{rev}$, where (k, ℓ) are coprime integers [63]. For the spin $s = 1$ case the locally minimum, but significantly large, entropy states occur at times (t_D, t_E, t_F, t_G) in Fig. 2(a). The P_Q representation, say, at time t_D [Fig. 3(a)] is bilocalized in two approximately antipodal domains of the spherical phase space. As the spin increases, more complex localized phase-space distributions start appearing due to the feasibility of wider distribution of the eigenvalues of the density matrix ρ_Q generated at these entropy minimum configurations. For the spin $s = \frac{3}{2}$ case we investigate the evolving state at time (t_D) considered in Fig. 4(a). The corresponding spin P_Q representation [Fig. 5(a)] depicts a 3-localized distribution of the quasiprobability density.

For a quantitative comparison of the localization achieved at various states during the evolution we adopt the measure of complexity introduced in [64], and utilized by authors of Ref. [65] for analyzing the spin phase-space distributions. Employing the second moment of the non-negative qudit $\mathrm{Q}_Q(\theta,\phi)$ function it represents the effective phase-space volume occupied by the quantum state:

$$W_2(\mathrm{Q}_Q) = [M_2(\mathrm{Q}_Q)]^{-1}, \quad M_2(\mathrm{Q}_Q) = \int (\mathrm{Q}_Q(\theta,\phi))^2 \, d\Omega. \quad (5.5)$$

The evaluations of $W_2(\mathrm{Q}_Q)$ quoted in Tables I and II suggest that compared to the spin kitten type states and other localized states, the high-entropy configurations [marked, for instance, by black broken lines in Figs. 2(a) and 4(a)] involve wider spread of phase-space distributions.

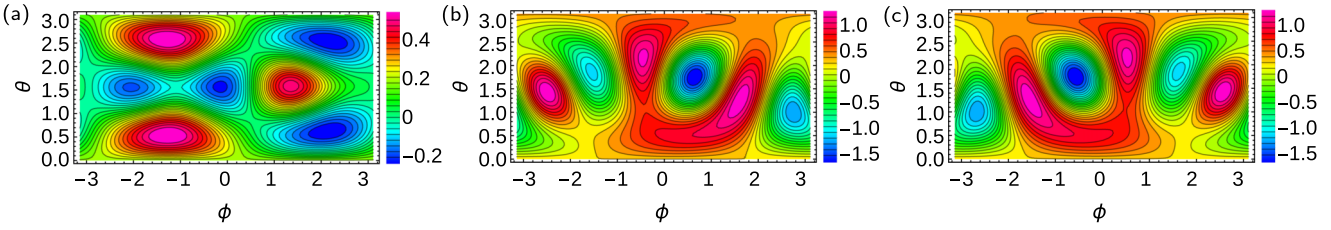

FIG. 5. For the initial state (3.1) with c = 0 we produce the spin quasiprobability $\mathrm{P}_{\mathcal{Q}}(\theta,\phi)$ representation for the $s=\frac{3}{2}$ case at various times considered in Fig. 4(a). The parametric choices here are identical to those in Fig. 4(a). The generalized spin kitten states arising at times t_{A} and t_{B}, when almost zero-entropy configurations trigger formation of nearly pure states, are illustrated in diagrams (b) and (c), respectively. Reconstruction of these states is discussed in Table III. The locally minimum, but significantly large, entropy structure realized at time t_{D} produces 3-localized spin state [diagram (a)] represented by a mixed-state density matrix.

Following our explicit verification (Fig. 9) of the effectiveness of the adiabatic approximation for the ultrastrong coupling domain $\widetilde{\lambda}\sim O(10^{-1})$ under the restriction of the present parametric regime, we consider the corresponding evolution of the entropy [Figs. 2(c) and 4(c)]. In contrast to the preceding discussion, the ultrastrong coupling domain incorporates a large number of interaction modes and their harmonics with a wide range of characteristic timescales $O\{[\frac{\Delta}{\omega}\exp(-\frac{\widetilde{\lambda}^2}{2})\widetilde{\lambda}^{2n}]^{-1}\}$, where $n\in(0,1,2,\ldots)$. As a consequence, the phase correlations among the interacting modes in the system are lost causing the disappearance of any collapse and revival pattern. The randomization of the phases induces the quasiperiodicity of the qudit entropy to vanish, and the system *does not return* close to its initial configuration in a finite time. A stabilization of the value of entropy [Figs. 2(c) and 4(c)] sets in, while a random stochastic fluctuation around the stabilized value of entropy is also observed.

VI. NONCLASSICAL FEATURES IN THE PHASE SPACE

A. Generalized spin kitten states

In general, the spin kitten type states may be understood as a linear superposition of suitably small number of spin coherent states. These pure state density matrices are characterized by zero value of the qudit entropy. An observation of Figs. 2(a) and 4(a) suggests that during the dynamical evolution the near-null values of entropy are recurrently reproduced at integral multiples of the quasiperiod (5.2). In addition, if these instances *do not* correspond to full revival (5.4), then the respective states reside, as measured by the metric (5.3), significantly far away from the factorized initial state. The descriptions following Figs. 2(a) and 4(a) suggest that the Hilbert-Schmidt distances between the states in question and the corresponding initial states maintain an order of magnitude estimate of the metric: $d_{\mathrm{HS}}(\rho_{\mathcal{Q}}(t_0),\rho_{\mathcal{Q}}(t))\sim O(1)$. Moreover, as these states are realized at locally minimum values of entropy during the evolution, they are relatively stable. To quantitatively characterize these approximate generalized spin kitten states, we consider their reconstruction via a variational technique based on minimization of the Hilbert-Schmidt distance between the dynamical state and a trial state comprising of a pure part, and an accompanying small component of a mixed state:

$$\widetilde{\rho}_{\mathcal{Q}}^{(s)}=\tau\left(\widetilde{\rho}_{\mathcal{Q}}^{(s)}\right)_{\mathrm{pure}}+(1-\tau)\left(\widetilde{\rho}_{\mathcal{Q}}^{(s)}\right)_{\mathrm{mixed}},\quad 0\leqslant\tau\leqslant 1, \tag{6.1}$$

where the index τ measures the purity of the reconstructed state. The pure density matrix in (6.1) employs an ensemble of $p'(>1)$ superposed spin coherent states:

$$\left(\widetilde{\rho}_{\mathcal{Q}}^{(s)}\right)_{\mathrm{pure}}=|\Psi\rangle\langle\Psi|,\quad |\Psi\rangle=\sum_{k=1}^{p'}c_k\,|\mathfrak{z}_k'\rangle,$$
$$\mathfrak{z}_k'=\tan\left(\frac{\theta_k'}{2}\right)\exp(-i\phi_k'),\quad \langle\Psi|\Psi\rangle=1. \tag{6.2}$$

The state $|\Psi\rangle$ in the above construction represents generalized spin kitten state. Making a slight departure from the standard [26,27] display of kitten states we admit in the construction given above unequal values of the norm of the complex coefficients $\{c_k\}$. Our generalized spin kitten states, therefore, contain asymmetrical superposition of spin coherent states. The mixed-state component (6.1) contains a convex combination of p'' spin coherent state density matrices:

$$\left(\widetilde{\rho}_{\mathcal{Q}}^{(s)}\right)_{\mathrm{mixed}}=\sum_{\ell=1}^{p''}g_\ell\,|\mathfrak{z}_\ell''\rangle\langle\mathfrak{z}_\ell''|,$$
$$\mathfrak{z}_\ell''=\tan\left(\frac{\theta_\ell''}{2}\right)\exp(-i\phi_\ell''),\quad 0\leqslant g_\ell\leqslant 1,$$
$$\sum_{\ell=1}^{p''}g_\ell=1. \tag{6.3}$$

TABLE I. For the $s=1$ case, we compute the complexity variable W_2 measuring the occupancy of the phase space at the locally minimal entropy configurations, and at a time $t=1.941\,000\times10^6$ [black broken line in Fig. 2(a)] when the entropy attains a near-maximal value: $S(\rho_{\mathcal{Q}}^{(1)})=1.038\,41$. The complexity value increases with the increment of the entropy of the state indicating the consequent larger spread of the quasiprobability density on the qudit phase space.

Time given in Fig. 2(a)	t_{D}	t_{A}	t_{B}	t_{C}	1.941×10^6
Complexity: $W_2(\mathrm{Q}_{\mathcal{Q}})$	11.95705	8.38795	10.45519	8.35376	12.39729

TABLE II. The complexity measure W_2 is computed for $s = \frac{3}{2}$ case at times when the mixed localized qudit state (t_D) as well as the nearly pure generalized spin kitten states (t_A, t_B) form. For comparison, the measure is also provided at time $t = 1.189\,300 \times 10^6$ [black broken line in Fig. 4 (a)], when the increased value of entropy $S(\rho_{\mathcal{Q}}^{(\frac{3}{2})}) = 1.222\,53$ causes a spreading of the spin $Q_{\mathcal{Q}}$ function.

Time given in Fig. 4(a)	t_D	t_A	t_B	1.1893×10^6
Complexity: $W_2(Q_Q)$	11.54365	9.09614	9.15175	11.58050

The identifying parameters $(\tau, p', \{c_k\}, \{\mathfrak{z}'_k\}, p'', \{g_\ell\}, \{\mathfrak{z}''_\ell\})$ of the marker state (6.1) are varied to enact a numerical minimization of the Hilbert-Schmidt distance between the investigated state appearing at specified time and its trial reconstruction: $d_{HS}(\rho_{\mathcal{Q}}^{(s)}(t), \widetilde{\rho}_{\mathcal{Q}}^{(s)})$. Our results are summarized in Table III. Towards pursuing the said numerical minimization process we start with the least number of real parameters required for reconstruction. For instance, if the entropy of the evolving qudit state at a particular time has near-null value and three peaks are evident in the $P_{\mathcal{Q}}$ representation, then an obvious candidate for the construction of its marker state (6.1)–(6.3) is given by superposition of three spin coherent states constituting the overwhelmingly large pure component, while a smaller contribution of the mixed-state density matrix is added to facilitate the minimization process. Moreover, close proximity of the values of the complexity variable (5.5) of the dynamical state and its trial entry serves as another benchmark of the selection process. This acts as a useful check against, say, a wrong choice of the value of p'. In the iterative optimization process we have varied two real parameters at a time. The iterations are continued until the Hilbert-Schmidt distance achieves a converged value. If the above minimization process indicates a linear superposition of p' spin coherent states in the reconstruction of the vector $|\Psi\rangle$ given in (6.2), we refer to the corresponding density matrix as the generalized p'-spin kitten state.

Another pertinent feature regarding the formation of generalized spin kitten states is their lifetime. The period of existence of these states is specifically marked in Figs. 2(b) and 4(b). For our parametric range these transient states live approximately for time span $O(10^4)$. We observe that decreased values of qudit gap (Δ) as well as the coupling strength (λ) lead to enhanced time of existence of the transitory spin kitten type states.

B. Second-order spin correlation function

Towards further study on the coherence properties of the nearly pure kitten type and other localized mixed qudit states we use the normalized second-order spin correlation function [23,27] defined as

$$g_s(t) = \frac{\langle S_+^2 S_-^2 \rangle}{\langle S_+ S_- \rangle^2}, \qquad \langle \Theta \rangle \equiv \mathrm{Tr}[\rho_{\mathcal{Q}}(t)\,\Theta]. \tag{6.4}$$

The correlation function (6.4) determines [23] possible existence of antibunching effect in the emission spectrum of photons. When the initial state (3.1) reduces to a spin coherent state (3.3) for the c = 0 choice, the correlation function (6.4)

TABLE III. The first block of rows in the table describes the generalized spin kitten states ($s = 1$) depicted in Figs. 3(b)–3(d) corresponding to respective times (t_A, t_B, t_C) given in Fig. 2(a). Almost pure generalized kitten states formed here are expressed as superposition of two spin coherent states. The following block of rows reconstruct the kitten type states ($s = \frac{3}{2}$) observed in Figs. 5(b) and 5(c) appearing, consecutively, at times (t_A, t_B) [Fig. 4(a)]. These generalized kitten states embody superposition of three spin coherent states. Towards studying the formation of generalized kitten states when the initial state (3.1) is entangled, we consider the example $s = \frac{3}{2}$, c = i in the final row of the table. The nearly pure spin kitten type state observed at t_A in Fig. 11(a_1) may be composed of a superposition of three spin coherent states. In all of the above reconstructions we add a small contribution of a coherent density matrix towards diminishing the metrical distance.

t	p', p''	$S(\rho_{\mathcal{Q}}^{(s)}(t)), S(\widetilde{\rho}_{\mathcal{Q}}^{(s)})$	τ	$\theta'_k \vert k = 1, \cdots, p'$	$\phi'_k \vert k = 1, \cdots, p'$	$c_k \vert k = 1, \cdots, p'$	$\theta''_\ell \vert \ell = 1, \cdots, p''$	$\phi''_\ell \vert \ell = 1, \cdots, p''$	$g_\ell \vert \ell = 1, \cdots, p''$	$d_{HS}(\rho_{\mathcal{Q}}^{(s)}(t), \widetilde{\rho}_{\mathcal{Q}}^{(s)})$
$s = 1$, c = 0										
t_A	2, 1	0.000077, 0.007227	0.998	1.144827,0.234039	−3.029563, 2.572028	−0.961961 − 0.712882i, 1.357050 + 0.120245i	0.100000	−3.141592	1	0.004913
t_B	2, 1	0.000160, 0.008293	0.998	0.602172,2.724220	−0.751886, 2.188110	−0.536977 − 0.474848i, 0.701177 − 0.062129i	1.690000	−2.240000	1	0.004322
t_C	2, 1	0.000208, 0.022903	0.996	1.784420,3.140420	−2.682160, 2.627840	−0.280798 − 0.918442i, 0.924292 + 0.081899i	0.750000	1.710000	1	0.005227
$s = \frac{3}{2}$, c = 0										
t_A	3, 1	0.001178, 0.035048	0.992	2.533350,0.252967,0.907040	1.653710,−0.406294, 0.683706	0.558771 + 0.378380i, 0.549972, 0.037398 + 0.523573i	0.160000	0	1	0.022958
t_B	3, 1	0.000819, 0.022226	0.995	2.521100, 0.542830, 3.139820	−2.707050, 0.046132, 0.836132	−0.064725 − 0.527516i, 0.576061 + 0.546934i, 0.313921 + 0.330102i	0.750000	0	1	0.015768
$s = \frac{3}{2}$, c = i										
t_A	3, 1	0.140408, 0.130252	0.947	2.752070, 0.607449, 3.026610	−2.841180, −3.001179, 0.808821	−0.786285i, 0.709199 + 0.246678i, 0.981572 + 0.544747i	2.340478	−0.532895	1	0.028934

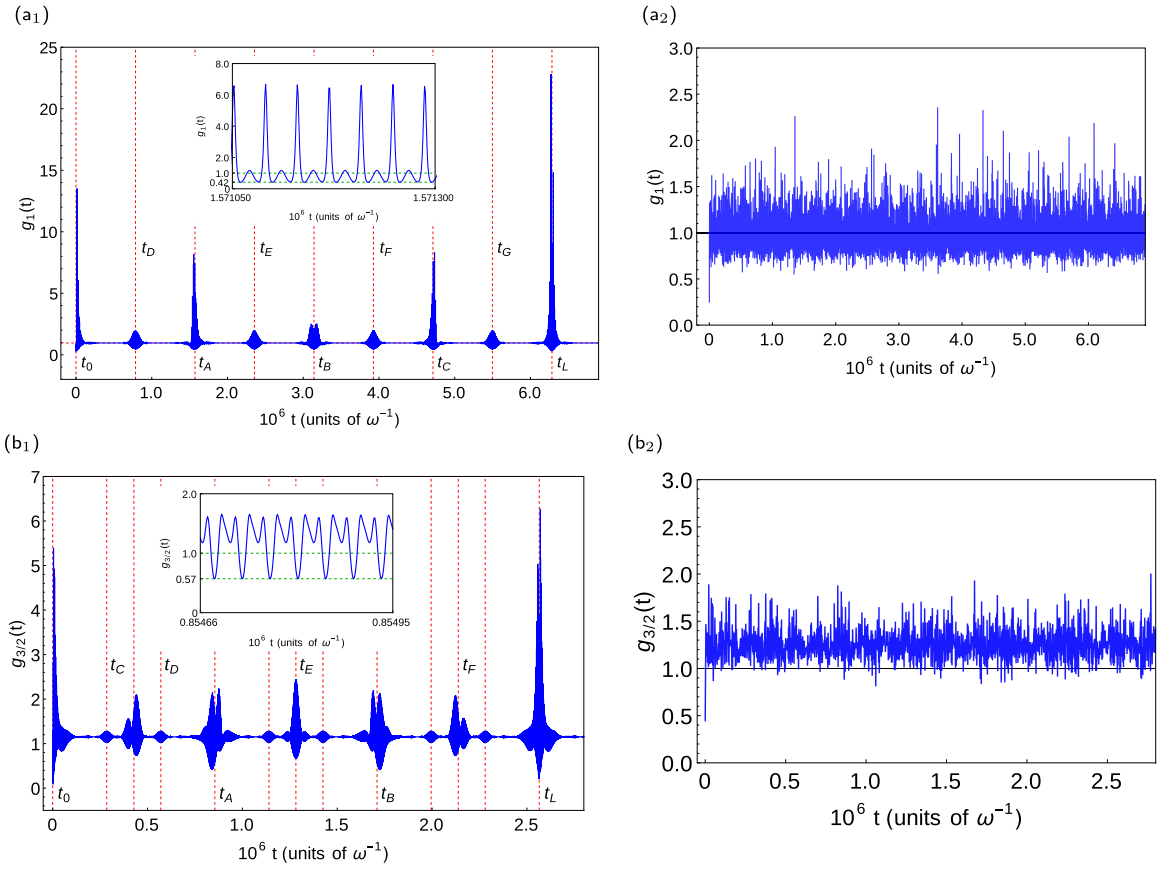

FIG. 6. For the factorized initial state (3.1) with c = 0 the time evolution of the second-order correlation function $g_s(t)$ is studied. For the $s = 1$ case in the strong coupling regime considered in the diagram (a_1), the coupling strength, other parameters, and the marked times of revival are taken to be identical to those in Fig. 2(a). Similarly the diagram (b_1) depicts the correlation function for the example $s = \frac{3}{2}$ where the coupling strength, other parametric values, and the times of total as well as fractional revivals are exactly same as those in Fig. 4(a). Compared to the other instances of revival, the fluctuations in $g_s(t)$ as observed for 3-localized mixed qudit states at times t_C, t_D in (b_1) are lesser as the corresponding dips in the entropy [Fig. 4(a)] are marginal. A distinctive feature between the insets in (a_1) and (b_1) reveals that the condition of antibunching of the emitted photons $g_s(t) < 1$ is more strongly satisfied for the lesser spin $s = 1$ case. Diagrams (a_2) and (b_2) study the incoherent chaotic behavior of $g_s(t)$ at the ultrastrong coupling regime $\widetilde{\lambda} = 0.2$. Other parametric values of (a_1)/(b_1) are retained in (a_2)/(b_2). Here also the validity of the antibunching condition occurs far more frequently for the lower-spin $s = 1$ example than its higher-spin analog.

reads as [66]

$$g_s(t=0) = \left(\frac{2s-1}{s}\right)\left[2s + \tan^2\left(\frac{\widetilde{\theta}}{2}\right)\right]^{-2} \times \left[\tan^4\left(\frac{\widetilde{\theta}}{2}\right) + 2(2s-1)\tan^2\left(\frac{\widetilde{\theta}}{2}\right) + s(2s-1)\right]. \tag{6.5}$$

In the strong coupling regime studied here, we explore the time dependence of the correlation function (6.4) to distinguish the temporal generalized kitten and other localized spin states from the residue characterized by high-entropy configurations noticed, say, in Figs. 2(a) and 4(a). The qudit density matrices for $s = 1$ and $\frac{3}{2}$ examples given in Eqs. (3.8) and (B7), respectively, now furnish the corresponding time-dependent spin correlation function (6.4). For the examples considered here, the function $g_s(t)$ given in (6.4) may be expressed via the ensemble averages listed below:

$$\begin{aligned}
\langle S_+S_-\rangle_{s=1} &= 2\sum_{n=0}^{\infty}\left(\left|\mathcal{B}^{(1)}_{+,n}(t)\right|^2 + \left|\mathcal{B}^{(1)}_{0,n}(t)\right|^2\right),\\
\langle S_+^2S_-^2\rangle_{s=1} &= 4\sum_{n=0}^{\infty}\left|\mathcal{B}^{(1)}_{+,n}(t)\right|^2,
\end{aligned} \tag{6.6}$$

$$\begin{aligned}
\langle S_+S_-\rangle_{s=\frac{3}{2}} &= \sum_{n=0}^{\infty}\left[3\left(\mathrm{B}^{(2,2)}_{n,n}(t) + \mathrm{B}^{(-1,-1)}_{n,n}(t)\right) + 4\mathrm{B}^{(1,1)}_{n,n}(t)\right],\\
\langle S_+^2S_-^2\rangle_{s=\frac{3}{2}} &= 12\sum_{n=0}^{\infty}\left(\mathrm{B}^{(2,2)}_{n,n}(t) + \mathrm{B}^{(1,1)}_{n,n}(t)\right).
\end{aligned} \tag{6.7}$$

The total and fractional revivals observed in the strong coupling domain [Figs. 6(a_1) and 6(b_1)] are symbolized by nearly sinusoidal, large-amplitude, and short-range oscillations in the time evolution of $g_s(t)$. These oscillations with time period

$\sim O(\omega^{-1})$ are visible in the insets of Figs. 6(a_1) and 6(b_1). Qualitatively, this may be understood as follows. These revival times are rational multiples of $T|_{\text{quasiperiod}}$ given in (5.2). At the time of revival there is a drop in entropy of the qudit. Relatively few modes of quantum fluctuations present at the instants of revival interfere coherently and give rise to transient harmonic fluctuations observed at those times. Away from these periods the qudit inhabits a highly mixed state and the entropy returns to its near-maximal value. For the high-entropy states a randomization of the phases of the fluctuation modes sets in. This, in turn, leads the oscillations to largely annihilate each other. This is evident [Figs. 6(a_1) and 6(b_1)] in the collapse of the fluctuations of the function $g_s(t)$ at instants off the revival times.

Another characteristic of the normalized correlation function $g_s(t)$ evident in Figs. 6(a_1) and 6(b_1) is that successive antibunching and bunching of the emitted radiation appear during the short-range coherent oscillations generated at the moments of revival. For the correlation function in the range $g_s(t) < 1$ ($g_s(t) > 1$) antibunching (bunching) of the emission process takes place. On the occasions of antibunching of the radiation the photoevents are said to be anticorrelated, i.e., occurrence of one makes the next one less likely. Oscillations observed in the correlation function $g_s(t)$ at the instants of revival [insets of Figs. 6(a_1) and 6(b_1)] demonstrate the consecutive display of antibunching and bunching effects. Collective interaction of the atoms with the photon field is known [23] to diminish the antibunching of radiation. In our context, it is revealed in a comparison of the insets in Figs. 6(a_1) and 6(b_1). For the spin $s = \frac{3}{2}$ example the minima of $g_s(t)$ achieved during revivals are comparatively higher than those realized for spin $s = 1$ case. This points towards the reduction of antibunching effects with increasing spin.

As observed before the ultrastrong coupling domain $\widetilde{\lambda} \lesssim O(1)$ generates a progressively large number of interaction modes with widely distributed characteristic timescales. As a consequence, the phase correlations among the interacting modes endowed with incommensurate frequencies are completely lost. The randomization of the phases eliminates all quasiperodic patterns. In particular, the time evolution of $g_s(t)$ in this domain exhibits [Figs. 6(a_2) and 6(b_2)] chaotic behavior without any quantum collapse and revival structure. In this fully randomized realm it is, however, observed [Figs. 6(a_2) and 6(b_2)] that for the $s = 1$ case, in contrast to the higher spin $s = \frac{3}{2}$ example, the correlation function exhibits $g_s(t) < 1$ property far more frequently. Therefore, the antibunching effect on the emitted photons survives in the chaotic regime for the low-spin qudits, and gradually disappear for larger spin quantum numbers where cooperative effects among the atoms become increasingly dominant.

C. Generation of spin-squeezed states

In order to study the emergence of the spin-squeezed states during the time evolution of the qudit-oscillator system, we follow the description given by the authors of Ref. [34]. The spin is regarded [34] to be squeezed if the variance of one spin component, perpendicular to the mean spin vector determined by the density matrix, assumes less value than the variance for a spin coherent state. The mean spin direction and its normal vectors are specified [37,45] via the following ordered triplet:

$$\begin{aligned}\vec{n}_1 &\equiv (\sin\vartheta\cos\varphi, \sin\vartheta\sin\varphi, \cos\vartheta),\\ \vec{n}_2 &\equiv (-\sin\varphi, \cos\varphi, 0),\\ \vec{n}_3 &\equiv (-\cos\vartheta\cos\varphi, -\cos\vartheta\sin\varphi, \sin\vartheta),\end{aligned} \tag{6.8}$$

where the polar and azimuthal angles are determined by the spin expectation values:

$$\vartheta = \cos^{-1}\frac{\langle S_z\rangle}{|\langle\vec{S}\rangle|},\quad \varphi = \begin{cases}\cos^{-1}\frac{\langle S_x\rangle}{|\langle\vec{S}\rangle|\sin\vartheta} & \text{if } \langle S_y\rangle > 0,\\ 2\pi - \cos^{-1}\frac{\langle S_x\rangle}{|\langle\vec{S}\rangle|\sin\vartheta} & \text{if } \langle S_y\rangle \leqslant 0.\end{cases} \tag{6.9}$$

In (6.9) we have used the notation $|\langle\vec{S}\rangle| = \sqrt{\langle S_x\rangle^2 + \langle S_y\rangle^2 + \langle S_z\rangle^2}$. An arbitrary vector normal to the mean spin direction reads as $\vec{n}_\perp = \vec{n}_2\cos\chi + \vec{n}_3\sin\chi$, and the corresponding spin component is given by $S_\perp \equiv \vec{S}\cdot\vec{n}_\perp$. The defining property (6.9) imposes the constraint $\langle S_\perp\rangle = 0$, and, therefore, the dispersion of the normal spin component reads as $(\Delta S_\perp)^2 = \langle S_\perp^2\rangle$. Using the notation $S_{\vec{n}_k} = \vec{S}\cdot\vec{n}_k$, $k \in \{2, 3\}$ the minimum variance of the normal spin component is now given by [37,45]

$$\begin{aligned}\min(\Delta S_\perp)^2 = \tfrac{1}{2}\big(\langle S_{\vec{n}_2}^2\rangle + \langle S_{\vec{n}_3}^2\rangle\big) - \tfrac{1}{2}\Big[\big(\langle S_{\vec{n}_2}^2\rangle - \langle S_{\vec{n}_3}^2\rangle\big)^2\\ + \big\langle\big(S_{\vec{n}_2}S_{\vec{n}_3} + S_{\vec{n}_3}S_{\vec{n}_2}\big)\big\rangle^2\Big]^{\frac{1}{2}}.\end{aligned} \tag{6.10}$$

The spin-squeezing measure provided in Ref. [34] is the ratio of the above minimum dispersion with the corresponding variance in a spin coherent state: $\xi_s^2 = \frac{2\min(\Delta S_\perp)^2}{s}$. The spin squeezing is realized [34] when the quantum correlation reduces the fluctuations in one spin component normal to the mean spin direction less than its coherent state limit.

In the presence of the spin squeezing, a quasiprobability density, say, the Wigner $W_{\mathcal{Q}}$ distribution, assumes an elliptical shape in contrast to an isotropic form that is evident for a spin coherent state. Quantum uncertainties are deformed by effective nonlinear interactions that twist the fluctuations as observed in Fig. 7. Nonlinear interactions triggering the spin-squeezing effect are produced in the low-energy limit of the effective Hamiltonian for the bipartite interaction (2.1) considered here. For instance, adopting the technique developed in [67] we may obtain the lowest order of nonlinear interactions in the present model, which, in particular, includes a term $\sim\omega\widetilde{\lambda}^2 S_z^2$ that activates one axis twisting of the quasiprobability densities. This effective Hamiltonian has also been achieved [53] using another technique. The mean spin direction and the optimal squeezing direction vary with time. We also note that accompanying the spin squeezing various degrees of eddylike structures are present in the $W_{\mathcal{Q}}$ distribution. The dominance of the said swirl causes limitations in the minimum attainable uncertainty, which, in turn, gives rise to relatively higher values of the squeezing parameter ξ_s^2. For the $s = 1$ and $\frac{3}{2}$ examples we study the evolutionary behavior of the squeezing parameter ξ_s^2 in Fig. 7. With the choice $c = 0$, the factorized initial state (3.1) does not experience any squeezing at $t = 0$ (Fig. 7). Owing to the nonlinear terms in the effective Hamiltonian, squeezing develops dynamically for the evolving state.

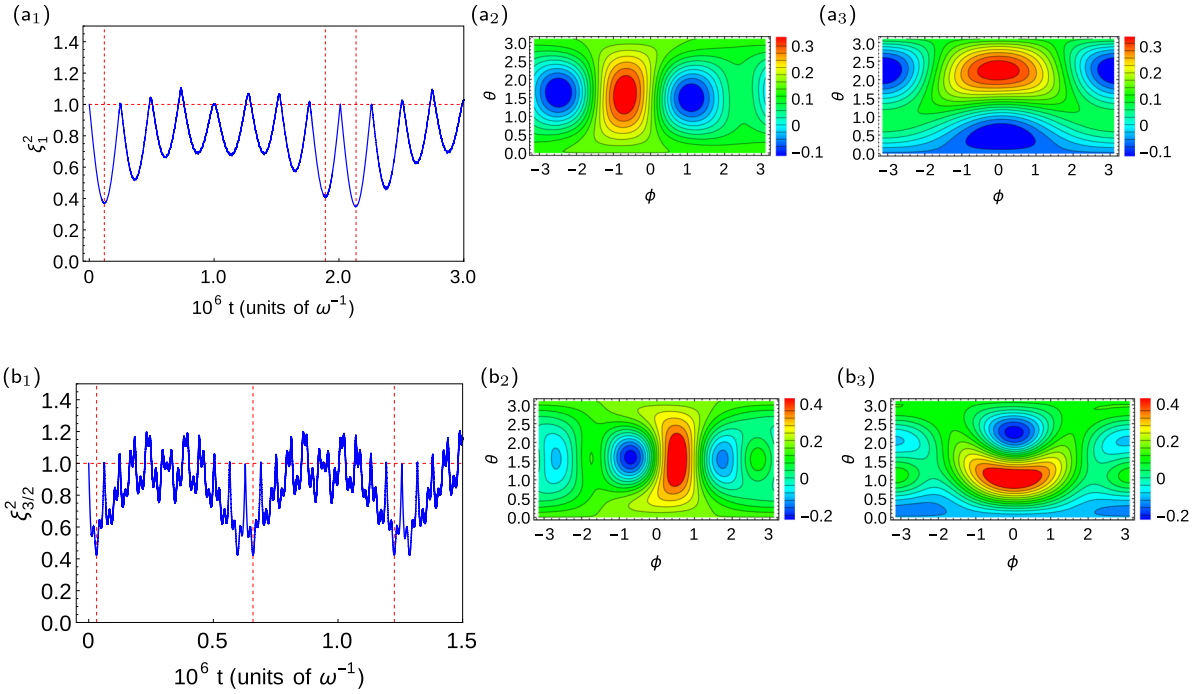

FIG. 7. The qudit Wigner $W_{\mathcal{Q}}$ distributions are plotted for the initial state (3.1) with c = 0, which represent a spin coherent state. (a) First row refers to spin $s = 1$ case with the parametric choices $\Delta = 0.12$, $\widetilde{\lambda} = 0.005$, $\mathfrak{z} = 0.3249$, $\alpha = 0.5$, $r = 0$. Diagram (a_1) depicts the long time evolution of the squeezing parameter, while (a_2) and (a_3) refer, consecutively, to $W_{\mathcal{Q}}$ distributions at times $t = 0.120\,717 \times 10^6$, $t = 2.137\,004 \times 10^6$. The corresponding squeezing coefficients equal $\xi_1^2 = 0.3712$ and 0.3492. (b) The $W_{\mathcal{Q}}$ distributions displayed in the second row study the $s = \frac{3}{2}$ example. Other parameters read as $\Delta = 0.1$, $\widetilde{\lambda} = 0.01$, $\mathfrak{z} = 0.3249$, $\alpha = 0.5$, $r = 0$. The long time evolution of the squeezing parameter is portrayed in (b_1), whereas (b_2) and (b_3) represent $W_{\mathcal{Q}}$ distributions at respective times $t = 0.031\,685 \times 10^6$, $t = 0.659\,013 \times 10^6$ with the corresponding squeezing coefficients given by $\xi_{\frac{3}{2}}^2 = 0.4242$ and 0.4223.

VII. QUANTUM SPIN STATE TOMOGRAPHY

In the previous sections we have described the evolution of the interacting spin-oscillator system via the phase-space quasiprobability distributions. Various tomographic schemes, however, develop representations of quantum states of systems in terms of the measurable normalized probability densities. Advancing a formulation of tomography of the spin states, the authors of Ref. [51] produced an invariant expression for the elements of the density matrix of spin s via a kernel function that is a measurable probability. The probability distribution function is a diagonal density matrix element of the spin state in an arbitrarily rotated frame described by the corresponding Euler angles denoted below as $(\mathfrak{a}, \mathfrak{b}, \mathfrak{g})$.

To describe the tomography scheme for the discrete spin variable, the authors of Refs. [51,52] employed the Wigner D matrices expressing the matrix elements of the irreducible representations of the rotation group:

$$\mathrm{D}^{j}_{m'm}(\mathfrak{a}, \mathfrak{b}, \mathfrak{g}) = \exp(i\mathfrak{a}m')\,\exp(i\mathfrak{g}m)\,d^{j}_{m'm}(\mathfrak{b}),$$
$$d^{j}_{m'm}(\mathfrak{b}) = \sqrt{\frac{(j+m')!(j-m')!}{(j+m)!(j-m)!}}\left(\cos\frac{\mathfrak{b}}{2}\right)^{m'+m}\left(\sin\frac{\mathfrak{b}}{2}\right)^{m'-m} P_{j-m'}^{m'-m,m'+m}(\cos\mathfrak{b}), \tag{7.1}$$

where the Jacobi polynomials [58] are given by $P_\ell^{\mathsf{a},\mathsf{b}}(x) = \sum_k \binom{\ell+\mathsf{a}}{\ell-k}\binom{\ell+\mathsf{b}}{k}(\frac{x-1}{2})^k(\frac{x+1}{2})^{\ell-k}$. Parametrized by Euler angles, the diagonal entries of the qudit density matrix provide [51,52] a positive-definite probability distribution of the allowed spin components in a direction specified by the corresponding rotations:

$$\widetilde{\omega}^{(s)}(m; \mathfrak{a}, \mathfrak{b}, \mathfrak{g}) \equiv \sum_{m',\, m''=-s}^{s} \mathrm{D}^{s}_{m\,m'}(\mathfrak{a}, \mathfrak{b}, \mathfrak{g})\,(\rho_{\mathcal{Q}})^{(s)}_{m'\,m''}\,\mathrm{D}^{s}_{m\,m''}(\mathfrak{a}, \mathfrak{b}, \mathfrak{g})^{*}. \tag{7.2}$$

As the discrete probability distribution (7.2) is constructed via utilizing the representation (7.1) of the rotation group, its dependence on the Euler angle $\mathfrak{a}$ disappears:

$$\widetilde{\omega}^{(s)}(m; \mathfrak{a}, \mathfrak{b}, \mathfrak{g}) \equiv \omega^{(s)}(m; \mathfrak{b}, \mathfrak{g}), \quad \sum_{m=-s}^{s} \omega^{(s)}(m; \mathfrak{b}, \mathfrak{g}) = 1. \tag{7.3}$$

In the example studied here, the construction (7.2) may be directly implemented as the evolution of the qudit density matrix is known under the adiabatic approximation scheme. For instance, the qudit density matrix (3.8) for $s = 1$ case immediately provides the corresponding tomogram that may be considered as the reconstruction of the state via the positive-definite probability distribution:

$$\begin{aligned}\omega^{(1)}(m;\mathfrak{b},\mathfrak{g}) = \frac{1}{2}\left(\frac{\sin\mathfrak{b}}{2}\right)^{2m}(1-m)!(1+m)!\sum_{n,\widetilde{n}=0}^{\infty}\Bigg\{\left(\cot\frac{\mathfrak{b}}{2}\;\; P_{1-m}^{m-1,m+1}(\cos\mathfrak{b})\right)^2\\ \times\mathcal{B}_{+,n}^{(1)}(t)\mathcal{B}_{+,\widetilde{n}}^{(1)}(t)^*\,\delta_{n\widetilde{n}}+\left(\tan\frac{\mathfrak{b}}{2}\;\; P_{1-m}^{m+1,m-1}(\cos\mathfrak{b})\right)^2\mathcal{B}_{-,n}^{(1)}(t)\mathcal{B}_{-,\widetilde{n}}^{(1)}(t)^*\delta_{n\widetilde{n}}\\ +2\left[P_{1-m}^{m,m}(\cos\mathfrak{b})\right]^2\mathcal{B}_{0,n}^{(1)}(t)\mathcal{B}_{0,\widetilde{n}}^{(1)}(t)^*\,\delta_{n\widetilde{n}}+2\sqrt{2}P_{1-m}^{m,m}(\cos\mathfrak{b})\Big[\tan\frac{\mathfrak{b}}{2}\\ \times P_{1-m}^{m+1,m-1}(\cos\mathfrak{b})\mathrm{Re}\big(\exp(i\mathfrak{g})\mathcal{B}_{0,n}^{(1)}(t)\mathcal{B}_{-,\widetilde{n}}^{(1)}(t)^*\,\mathcal{G}_{\widetilde{n}n}(-\widetilde{\lambda})\big)+\cot\frac{\mathfrak{b}}{2}\\ \times P_{1-m}^{m-1,m+1}(\cos\mathfrak{b})\mathrm{Re}\big(\exp(i\mathfrak{g})\mathcal{B}_{+,n}^{(1)}(t)\mathcal{B}_{0,\widetilde{n}}^{(1)}(t)^*\,\mathcal{G}_{\widetilde{n}n}(-\widetilde{\lambda})\big)\Big]\\ +2\,P_{1-m}^{m-1,m+1}(\cos\mathfrak{b})P_{1-m}^{m+1,m-1}(\cos\mathfrak{b})\mathrm{Re}\Big(\exp(2i\mathfrak{g})\\ \times\mathcal{B}_{+,n}^{(1)}(t)\mathcal{B}_{-,\widetilde{n}}^{(1)}(t)^*\,\mathcal{G}_{\widetilde{n}n}(-2\widetilde{\lambda})\Big)\Bigg\}.\end{aligned}\tag{7.4}$$

Continuing further, we also employ our approximate evaluation of the $s=\frac{3}{2}$ qudit density matrix given in (B7) to procure the corresponding tomogram:

$$\begin{aligned}\omega^{(\frac{3}{2})}(m;\mathfrak{b},\mathfrak{g}) = \frac{1}{6}\left(\frac{\sin\mathfrak{b}}{2}\right)^{2m}\left(\frac{3}{2}-m\right)!\left(\frac{3}{2}+m\right)!\sum_{n,\widetilde{n}=0}^{\infty}\Bigg\{\delta_{n\widetilde{n}}\Big[\cot^3\frac{\mathfrak{b}}{2}\left(P_{\frac{3}{2}-m}^{m-\frac{3}{2},m+\frac{3}{2}}(\cos\mathfrak{b})\right)^2\mathrm{B}_{n,\widetilde{n}}^{(2,2)}(t)\\ +3\cot\frac{\mathfrak{b}}{2}\left(P_{\frac{3}{2}-m}^{m-\frac{1}{2},m+\frac{1}{2}}(\cos\mathfrak{b})\right)^2\mathrm{B}_{n,\widetilde{n}}^{(1,1)}(t)+3\tan\frac{\mathfrak{b}}{2}\left(P_{\frac{3}{2}-m}^{m+\frac{1}{2},m-\frac{1}{2}}(\cos\mathfrak{b})\right)^2\mathrm{B}_{n,\widetilde{n}}^{(-1,-1)}(t)\\ +\tan^3\frac{\mathfrak{b}}{2}\left(P_{\frac{3}{2}-m}^{m+\frac{3}{2},m-\frac{3}{2}}(\cos\mathfrak{b})\right)^2\mathrm{B}_{n,\widetilde{n}}^{(-2,-2)}(t)\Big]+2\sqrt{3}\;P_{\frac{3}{2}-m}^{m-\frac{3}{2},m+\frac{3}{2}}(\cos\mathfrak{b})\Big[\cot^2\frac{\mathfrak{b}}{2}\\ \times P_{\frac{3}{2}-m}^{m-\frac{1}{2},m+\frac{1}{2}}(\cos\mathfrak{b})\;\mathrm{Re}\big(\exp(i\mathfrak{g})\,\mathrm{B}_{n,\widetilde{n}}^{(2,1)}(t)\,\mathcal{G}_{\widetilde{n}n}(-\widetilde{\lambda})\big)+\cot\frac{\mathfrak{b}}{2}\;P_{\frac{3}{2}-m}^{m+\frac{1}{2},m-\frac{1}{2}}(\cos\mathfrak{b})\\ \times\mathrm{Re}\big(\exp(2i\mathfrak{g})\,\mathrm{B}_{n,\widetilde{n}}^{(2,-1)}(t)\,\mathcal{G}_{\widetilde{n}n}(-2\widetilde{\lambda})\big)\Big]+2\sqrt{3}\;P_{\frac{3}{2}-m}^{m+\frac{3}{2},m-\frac{3}{2}}(\cos\mathfrak{b})\Big[\tan^2\frac{\mathfrak{b}}{2}\\ \times P_{\frac{3}{2}-m}^{m+\frac{1}{2},m-\frac{1}{2}}(\cos\mathfrak{b})\;\mathrm{Re}\big(\exp(i\mathfrak{g})\,\mathrm{B}_{n,\widetilde{n}}^{(-1,-2)}(t)\,\mathcal{G}_{\widetilde{n}n}(-\widetilde{\lambda})\big)+\tan\frac{\mathfrak{b}}{2}\;P_{\frac{3}{2}-m}^{m-\frac{1}{2},m+\frac{1}{2}}(\cos\mathfrak{b})\\ \times\mathrm{Re}\big(\exp(2i\mathfrak{g})\,\mathrm{B}_{n,\widetilde{n}}^{(1,-2)}(t)\,\mathcal{G}_{\widetilde{n}n}(-2\widetilde{\lambda})\big)\Big]+2\;P_{\frac{3}{2}-m}^{m+\frac{3}{2},m-\frac{3}{2}}(\cos\mathfrak{b})\;P_{\frac{3}{2}-m}^{m-\frac{3}{2},m+\frac{3}{2}}(\cos\mathfrak{b})\\ \times\mathrm{Re}\big(\exp(3i\mathfrak{g})\,\mathrm{B}_{n,\widetilde{n}}^{(2,-2)}(t)\,\mathcal{G}_{\widetilde{n}n}(-3\widetilde{\lambda})\big)+6\;P_{\frac{3}{2}-m}^{m+\frac{1}{2},m-\frac{1}{2}}(\cos\mathfrak{b})\;P_{\frac{3}{2}-m}^{m-\frac{1}{2},m+\frac{1}{2}}(\cos\mathfrak{b})\\ \times\mathrm{Re}\big(\exp(i\mathfrak{g})\,\mathrm{B}_{n,\widetilde{n}}^{(1,-1)}(t)\,\mathcal{G}_{\widetilde{n}n}(-\widetilde{\lambda})\big)\Big\}.\end{aligned}\tag{7.5}$$

Towards expressing the phase-space quasiprobability densities via the true tomographic probability distribution explicitly determined here, one may proceed as follows. Applying the orthogonality relations of the Wigner $3j$ coefficients [48] the authors of Ref. [51] inverted the defining property (7.2) and expressed the qudit density matrix elements in the angular momentum basis via an integral over all possible rotations:

$$\begin{aligned}(-1)^{m''}(\rho_{\mathcal{Q}})_{m'm''}^{(s)} = \sum_{\sigma=0}^{2s}\sum_{\widetilde{m}=-\sigma}^{\sigma}(2\sigma+1)^2\sum_{m=-s}^{s}(-1)^m\begin{pmatrix}s & s & \sigma\\ m & -m & 0\end{pmatrix}\begin{pmatrix}s & s & \sigma\\ m' & -m'' & \widetilde{m}\end{pmatrix}\\ \times\int\omega^{(s)}(m;\mathfrak{b},\mathfrak{g})\,\mathrm{D}_{0\widetilde{m}}^{\sigma}(\mathfrak{a},\mathfrak{b},\mathfrak{g})\,\frac{d\mathcal{W}}{8\pi^2},\end{aligned}\tag{7.6}$$

where the measure of the angular variables is given by $\int d\mathcal{W} = \int_0^{2\pi} d\mathfrak{a}\int_0^{\pi}\sin\mathfrak{b}\,d\mathfrak{b}\int_0^{2\pi} d\mathfrak{g} = 8\pi^2$. Extending this approach, we use the tomographic composition (7.6) of the qudit state to express its density matrix in the spherical tensor basis (4.4) as

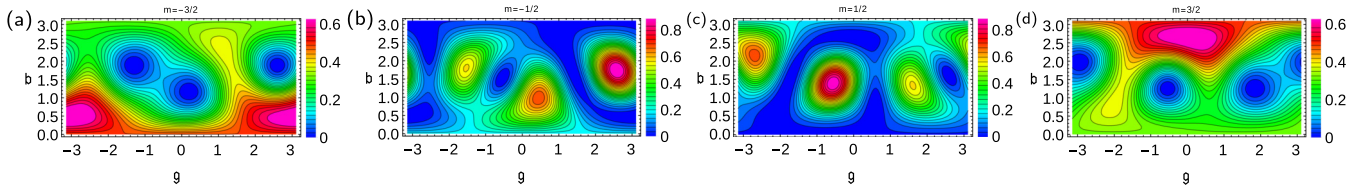

FIG. 8. The tomogram $\omega^{(\frac{3}{2})}(m;\mathfrak{b},\mathfrak{g})$ for the $s=\frac{3}{2}$ case is considered for the time $t_{\rm B}$ given in Fig. 4(a). The positive-definite probability distributions for spin projections $m=\pm\frac{1}{2}$ show the emergence of three peaks.

follows:

$$(\varrho^{\mathcal{Q}})^{(s)}_{k\,q}=(2\,k+1)^{\frac{3}{2}}\sum_{m}(-1)^{s-m+q}\begin{pmatrix}s & s & k\\ m & -m & 0\end{pmatrix}\int\omega^{(s)}\,(m;\mathfrak{b},\mathfrak{g})\,\mathrm{D}^{k}_{0\,-q}(\mathfrak{a},\mathfrak{b},\mathfrak{g})\,\frac{d\mathcal{W}}{8\,\pi^2}. \tag{7.7}$$

The above integral on the Euler angular variables admits a consistency check between our expressions of the tomograms evaluated in (7.4) and (7.5) for the respective cases $s=1,\frac{3}{2}$ on one hand, and the corresponding expressions of the qudit density matrix in the spherical tensor basis produced in (4.5) and (B10) on the other. The phase-space quasiprobabilities such as the qudit $\mathrm{P}_{\mathcal{Q}}$ representation, Wigner $\mathrm{W}_{\mathcal{Q}}$ distribution, and the $\mathrm{Q}_{\mathcal{Q}}$ function, given in Eqs. (4.8), (4.11), and (4.13), respectively, may now be explicitly formulated using the positive-definite probability distribution $\omega^{(s)}(m;\mathfrak{b},\mathfrak{g})$ associated with spin projections in arbitrarily rotated frames.

Towards demonstrating the tomographic representation of the qudit generalized kitten states we, for instance, examine the configuration at time $t_{\rm B}$ given in Fig. 4(a) for the $s=\frac{3}{2}$ example. The construction (7.5) yields the corresponding tomogram displayed in Fig. 8. Figures 8(a)–8(d) therein specify the probability distributions for the spin projections corresponding to the generalized qudit three-kitten state. The probability densities $\omega^{(\frac{3}{2})}(\pm\frac{1}{2};\mathfrak{b},\mathfrak{g})$ observed in Figs. 8(b) and 8(c) exhibit emergence of three uneven peak regions for this state, which, in turn, may be used to determine the qudit $\mathrm{P}_{\mathcal{Q}}$ representation via the structures (7.7) and (4.8).

VIII. CONCLUSION

Applying an adiabatic approximation method, we study a hybrid qudit-oscillator interacting system in the strong as well as the ultrastrong interaction regimes. Starting with a pure state of the bipartite system, we observe its evolution via the phase-space dynamics. The quasiprobability distributions in the hybrid factorized phase space are constructed. The corresponding distributions of one sector are procured from their hybrid analogs via a dimensional reduction process achieved by integrating the phase-space variables of the complementary sector. In the strong coupling domain, the system displays a quasiperiodic behavior when it returns close to its initial configuration. Excluding the near duplication of the initial state, other interesting possibilities also emerge during the evolution. Starting with a factorizable initial state we observe that at the local minimum values of the entropy, either almost pure generalized spin kitten states or mixed qudit states, which are, however, localized in the phase space, originate. The spin kitten type states are realized for the entropy constraint $S(\rho_{\mathcal{Q}})\ll 1$ that holds in conjunction with the metrical requirement $d_{\rm HS}(\rho_{\mathcal{Q}}(t=0),\rho_{\mathcal{Q}}(t))\sim O(1)$ for the states in question. On the other hand, mixed localized qudit states arise when the locally minimum entropy during the evolution satisfies the order-of-magnitude estimate $S(\rho_{\mathcal{Q}})\lesssim O[\ln(2s+1)]$. It has been argued in the context of (5.2) that up to the validity of our approximation the timescale of emergence $(\mathrm{T}|_{\rm quasiperiod})$ of the above spin states does not depend on s. In a large-s bipartite system, therefore, generalized nearly pure spin kitten states may be observed before the decohering effects destroy the phase correlations at a timescale $t\gg\mathrm{T}|_{\rm quasiperiod}$.

Another feature of nonclassicality observed is that due to presence of the quadratic terms of the spin generators in the effective Hamiltonian, the initial spin coherent state dynamically and recurrently evolves to squeezed spin states when the system undergoes quantum fluctuations. For the ultrastrong coupling strength, the quasiperiodicity of the evolution disappears and the entropy shows stabilization in the presence of a randomized fluctuation. Moreover, both in the strong and ultrastrong coupling regimes, antibunching of the emitted photons is observed particularly for the low-spin ($s=1$) case. We also note that it is important to estimate the extent of nonclassicality of the quantum states in the ultrastrong coupling regime [Figs. 2(c) and 4(c)] where an equilibriumlike behavior sets in. This will be pursued elsewhere.

Now, we briefly comment on the experimental observation of the nearly pure generalized spin kitten states discussed in this work. Specifically, experimental feasibility of high-precision tomographic reconstruction of a spin density matrix via repeated measurements on an ensemble of identical states has been discussed [68]. The reconstructed matrix elements involve statistical errors that can be made arbitrarily small [68] by increasing the number of observations. Experimental realization of complete quantum spin state tomography for quadrupolar nuclei by employing global rotations of the spin structure has been reported [69]. A tomographic map of the full density matrix of an exciton-based qubit in a single quantum dot has been demonstrated [70] by utilizing arbitrary rotation of the measurement basis. This reconstruction of the density matrix may be extended [70] to multiqubit systems. For the density matrices which are closely pure, a tomographic reconstruction that provides major performance improvement for large systems has been suggested [71]. A recent work achieved [72] experimental reconstruction of the

TABLE IV. Lists (a) and (b) compare the energy eigenvalues [insets in Figs. 9(a) and 9(b), sequentially] without and with the adiabatic approximation for the $s = 1$ and $\frac{3}{2}$ cases, respectively. For the list (a) the ultrastrong coupling is chosen as $\widetilde{\lambda} = 0.33$ [marked by black vertical dotted line in the inset of Fig. 9(a)], whereas the energy eigenvalues for the list (b) are analogously given for the coupling $\widetilde{\lambda} = 0.32$ [another black vertical dotted line in the inset of Fig. 9(b)]. Additional parameters in (a) and (b) are maintained equal to those in Figs. 9(a) and 9(b), respectively. The close proximity of the energy eigenvalues quoted here without and with the assumption of adiabatic approximation points towards the accuracy of the said approximation in the parametric range studied here.

	(a)				(b)			
$E^{(1)}_{j,n}$	$E^{(1)}_{-,9}$	$E^{(1)}_{0,9}$	$E^{(1)}_{+,9}$	$E^{\pm,\frac{3}{2}}_{\ell,n}$	$E^{-,\frac{3}{2}}_{+1,6}$	$E^{-,\frac{3}{2}}_{-1,6}$	$E^{+,\frac{3}{2}}_{+1,6}$	$E^{+,\frac{3}{2}}_{-1,6}$
Without approx.	8.88208	8.89332	9.00664	Without approx.	5.75043	5.76052	5.92712	6.04642
With adiabatic approx.	8.88202	8.89110	9.00908	With adiabatic approx.	5.74932	5.75813	5.92902	6.05153

quantum state of an electronic spin qubit linked to nitrogen-vacancy center in diamond at room temperature, and studied its nonclassicality by employing its Wigner W distribution on a spherical phase space. Time evolution of a quantum spin state undergoing a dephasing process has also been observed [72] in this system. In the context of the above experimental developments, a tomographic realization of the present transitory spin kitten type states may be possible. As our generalized kitten states are nearly pure, the mapping described in [71] is particularly relevant here, especially for higher-spin qudits. The evaluation of measurable probability densities in Sec. VII then admits a direct comparison with experiments.

ACKNOWLEDGMENTS

We are indebted for generous computational help from the Department of Central Instrumentation and Service Laboratory, University of Madras. One of us (M.B.) acknowledges the support from the University of Madras for granting a University Research Fellowship (No. GCCO/A6/TP/URF/2016/709). Another author (R.C.) wishes to thank the Department of Nuclear Physics, University of Madras, for kind hospitality.

APPENDIX A: VALIDITY OF THE ADIABATIC APPROXIMATION

Towards examining the accuracy of the adiabatic approximation in our parametric regime, we, following [46], now compare the low-lying energy eigenvalues extracted via the numerical diagonalization of the Hamiltonian (2.1) expressed in the basis set $\{|s, m; n_m\rangle\}$, and an alternate evaluation of the said eigenvalues by employing its reduction to the block-diagonal form [Eqs. (2.5) and (B1)] achieved under the approximation method described in Sec. II. For instance, in the $s = 1$ case, we may recast the Hamiltonian (2.1) utilizing the inner product of the displaced oscillator states as follows:

$$\begin{pmatrix}
 & & & 0 & -\widetilde{\Delta}\langle 1|0_{_1}\rangle & 0 & 0 & -\widetilde{\Delta}\langle 2|0_{_1}\rangle & 0 & \dots \\
 & H_0^{(s=1)} & & \widetilde{\Delta}\langle 1|0_{_1}\rangle & 0 & -\widetilde{\Delta}\langle 1_{_{-1}}|0\rangle & -\widetilde{\Delta}\langle 2|0_{_1}\rangle & 0 & -\widetilde{\Delta}\langle 2_{_{-1}}|0\rangle & \dots \\
 & & & 0 & \widetilde{\Delta}\langle 1_{_{-1}}|0\rangle & 0 & 0 & -\widetilde{\Delta}\langle 2_{_{-1}}|0\rangle & 0 & \dots \\
0 & \widetilde{\Delta}\langle 1|0_{_1}\rangle & 0 & & & & 0 & -\widetilde{\Delta}\langle 2|1_{_1}\rangle & 0 & \dots \\
-\widetilde{\Delta}\langle 1|0_{_1}\rangle & 0 & \widetilde{\Delta}\langle 1_{_{-1}}|0\rangle & & H_1^{(s=1)} & & \widetilde{\Delta}\langle 2|1_{_1}\rangle & 0 & -\widetilde{\Delta}\langle 2_{_{-1}}|1\rangle & \dots \\
0 & -\widetilde{\Delta}\langle 1_{_{-1}}|0\rangle & 0 & & & & 0 & \widetilde{\Delta}\langle 2_{_{-1}}|1\rangle & 0 & \dots \\
0 & -\widetilde{\Delta}\langle 2|0_{_1}\rangle & 0 & 0 & \widetilde{\Delta}\langle 2|1_{_1}\rangle & 0 & & & & \dots \\
-\widetilde{\Delta}\langle 2|0_{_1}\rangle & 0 & -\widetilde{\Delta}\langle 2_{_{-1}}|0\rangle & -\widetilde{\Delta}\langle 2|1_{_1}\rangle & 0 & \widetilde{\Delta}\langle 2_{_{-1}}|1\rangle & & H_2^{(s=1)} & & \dots \\
0 & -\widetilde{\Delta}\langle 2_{_{-1}}|0\rangle & 0 & 0 & -\widetilde{\Delta}\langle 2_{_{-1}}|1\rangle & 0 & & & & \dots \\
\vdots & \vdots & \vdots & \vdots & \vdots & \vdots & \vdots & \vdots & \vdots & \ddots
\end{pmatrix}, \tag{A1}$$

where the diagonal blocks follow from (2.5), and the scaled atomic frequency reads as $\widetilde{\Delta} = \frac{\Delta}{\sqrt{2}}$. The order of the rows and columns in (A1) is given by the set $\{|m; n_m\rangle | m = 1, 0, -1; n = 0, 1, \dots\}$. The approximation entails curtailing the matrix (A1) to its block-diagonal form [46] that may be justified in the $\Delta \ll \omega$ limit. Physically, it requires existence of a much shorter characteristic timescale of the oscillator compared to that of the slow-moving atom [47]. For the $s = \frac{3}{2}$ case exactly parallel structure as (A1) may be reproduced.

Figure 9(a) quantitatively provides the $\widetilde{\lambda}$ dependence of the approximate energy eigenvalues of the $s = 1$ Hamiltonian. For our numerical analysis, the Hamiltonian (A1) *containing* the off-diagonal submatrices is retained up to the 39×39 elements. Its diagonalization furnishes the low-lying energy eigenvalues computed numerically *without* application of the adiabatic approximation. At the next step, the approximation is implemented by discarding the off-block terms and truncating the Hamiltonian matrix (A1) to the block-diagonal form. A comparison of these *two* sets of nearly equal energy

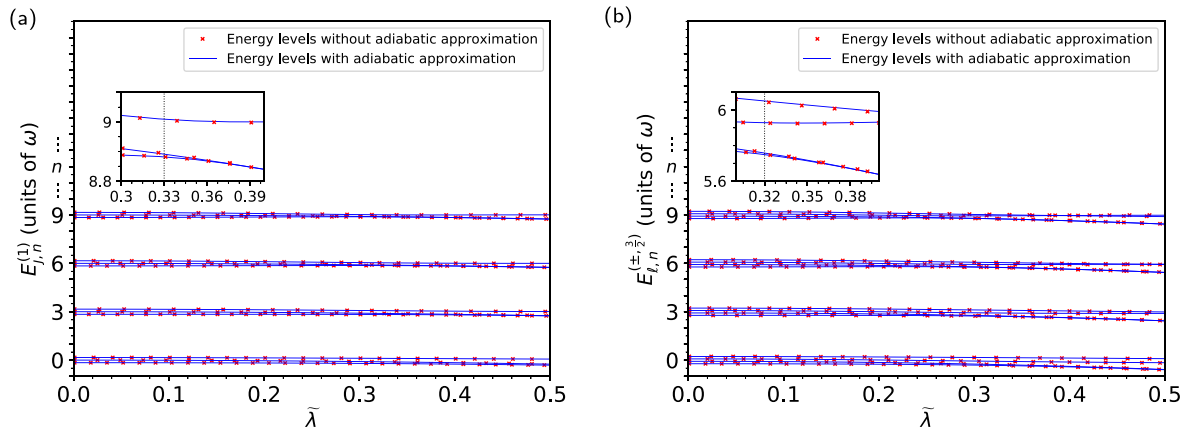

FIG. 9. The diagrams compare numerical solutions of low-lying energy levels obtained without assuming the adiabatic approximation (red crosses) to the corresponding levels computed under the said approximation (blue lines) in (a) and (b) for the $s = 1$ and $\frac{3}{2}$ examples, respectively. Interacting with the slow-moving qudit ($\Delta = 0.16$ for $s = 1$ and $\Delta = 0.15$ for $s = \frac{3}{2}$) the fast-moving oscillator ($\omega = 1$) sets up the scale making the approximation valid up to the ultrastrong coupling domain $\widetilde{\lambda} \lesssim 0.5$ considered here. Numerical estimates of the above two sets of energy eigenvalues for typical ultrastrong couplings [marked by vertical black dotted lines in the insets of diagrams (a) and (b)], obtained via the said dissimilar procedures, are listed in Tables IV(a) and IV(b), respectively.

eigenvalues in Fig. 9(a) up to the ultrastrong coupling regime $\widetilde{\lambda} \lesssim 0.5$ validates our claim on the accuracy of the adiabatic approximation in this domain. Sample numerical estimates of a set of eigenenergies employing the above two contrasting procedures for an ultrastrong coupling value, marked by a vertical black dotted line in the inset of Fig. 9(a), are quoted in Table IV(a). Analogously, for the choice $s = \frac{3}{2}$, the comparative structure of the two sets of energy eigenvalues, *without* and *with* the adiabatic approximation mechanism, is described in Fig. 9(b) [and Table IV(b)] up to the said ultrastrong coupling domain $\widetilde{\lambda} \lesssim 0.5$. For the numerical evaluation in the $s = \frac{3}{2}$ case sans [Fig. 9(b)] the adiabatic approximation we have considered 40×40 Hamiltonian matrix in the displaced oscillator basis $\{|m; n_m\rangle | m = \frac{3}{2}, \frac{1}{2}, -\frac{3}{2}, -\frac{1}{2}; n = 0, 1, \ldots\}$. Put together, the graphical representations in Fig. 9 suggest that in our domain of interest $\Delta \ll \omega$ the adiabatic approximation remains dependable in the strong and ultrastrong interaction regimes considered in this work. The large detuning sets apart the respective timescales of the qudit and the oscillator, and may be regarded as the underlying reason for the validity of the approximation. For the $s = 1$ case the adiabatic approximation has been applied before in Ref. [73] for an ultrastrong coupling value.

APPENDIX B: SPIN DENSITY MATRIX FOR $s = \frac{3}{2}$

Adhering to the recipe described in Sec. II, the adiabatic approximation for the spin $s = \frac{3}{2}$ example may be summarized as given below. The nth photonic block Hamiltonian now reads as

$$H_n^{(s=\frac{3}{2})} = \omega \begin{pmatrix} n - \left(\frac{3\widetilde{\lambda}}{2}\right)^2 & \sqrt{\frac{3}{2}}\Delta_n & 0 & 0 \\ \sqrt{\frac{3}{2}}\Delta_n & n - \left(\frac{\widetilde{\lambda}}{2}\right)^2 & \sqrt{2}\,\Delta_n & 0 \\ 0 & \sqrt{2}\,\Delta_n & n - \left(\frac{\widetilde{\lambda}}{2}\right)^2 & \sqrt{\frac{3}{2}}\Delta_n \\ 0 & 0 & \sqrt{\frac{3}{2}}\Delta_n & n - \left(\frac{3\widetilde{\lambda}}{2}\right)^2 \end{pmatrix}. \tag{B1}$$

The eigenenergies of the Hamiltonian (B1) are listed as

$$E^{\pm,\frac{3}{2}}_{\ell,n} = \omega\left(n - \frac{5\widetilde{\lambda}^2}{4} + \ell\,\frac{\Delta_n}{\sqrt{2}} \pm \chi_n^{(\ell)}\right),$$
$$\chi_n^{(\ell)} = \sqrt{\widetilde{\lambda}^4 + \ell\,\sqrt{2}\,\widetilde{\lambda}^2\,\Delta_n + 2\,\Delta_n^2}, \quad \ell \in \{\pm 1\}, \tag{B2}$$

while the corresponding eigenvectors read as

$$\left|E^{\pm,\frac{3}{2}}_{\ell,n}\right\rangle = \frac{1}{\mathcal{N}^{\pm,\frac{3}{2}}_{\ell,n}}\left(\left|\frac{3}{2}, \frac{3}{2}; n_{\frac{3}{2}}\right\rangle + \Gamma_\ell^{(\pm)}\left|\frac{3}{2}, \frac{1}{2}; n_{\frac{1}{2}}\right\rangle + \ell\,\Gamma_\ell^{(\pm)}\left|\frac{3}{2}, -\frac{1}{2}; n_{-\frac{1}{2}}\right\rangle + \ell\left|\frac{3}{2}, -\frac{3}{2}; n_{-\frac{3}{2}}\right\rangle\right) \tag{B3}$$

and the coefficients therein are given by

$$\Gamma_\ell^{(\pm)} = \frac{1}{\sqrt{3}}\left(\ell \pm \sqrt{2}\,\frac{\chi_n^{(\ell)} \pm \widetilde{\lambda}^2}{\Delta_n}\right), \mathcal{N}^{\pm,\frac{3}{2}}_{\ell,n} = \sqrt{2}[1 + (\Gamma_\ell^{(\pm)})^2]^{\frac{1}{2}}. \tag{B4}$$

The orthocompleteness relations for the states (B3) hold in the nth photonic sector: $\langle E^{\kappa',\frac{3}{2}}_{\ell',n} | E^{\kappa,\frac{3}{2}}_{\ell,n}\rangle = \delta_{\ell\ell'}\delta_{\kappa\kappa'}$ ($\kappa, \kappa' \in \{\pm\}$), and $\sum_{\ell,\kappa} |E^{\kappa,\frac{3}{2}}_{\ell,n}\rangle\langle E^{\kappa,\frac{3}{2}}_{\ell,n}| = \mathbb{I}$.

The basis states $|E^{\pm,\frac{3}{2}}_{\ell,n}\rangle$ listed in (B3) facilitate the approximate determination of the evolution of the initial state (3.1) for the spin $s = \frac{3}{2}$ case:

$$\left|\psi_{\frac{3}{2}}(t)\right\rangle = \sum_{\kappa\in\pm}\sum_{\ell\in\pm1}\sum_{n=0}^{\infty} \mathcal{A}^{\kappa,\frac{3}{2}}_{\ell,n}\exp\left(-iE^{\kappa,\frac{3}{2}}_{\ell,n}t\right)\left|E^{\kappa,\frac{3}{2}}_{\ell,n}\right\rangle,$$
$$\mathcal{A}^{\pm,\frac{3}{2}}_{\ell,n} \equiv \left\langle E^{\pm,\frac{3}{2}}_{\ell,n}\middle|\psi_{\frac{3}{2}}(0)\right\rangle, \tag{B5}$$

which, in turn, furnishes the corresponding pure state bipartite density matrix $\rho^{(s=\frac{3}{2})}(t) \equiv |\psi_{\frac{3}{2}}(t)\rangle\,\langle\psi_{\frac{3}{2}}(t)|$. The explicit evaluation

of the coefficients in (B5) reads as

$$\mathcal{A}^{\pm,\frac{3}{2}}_{\ell,n} = \frac{\mathcal{N}_{\frac{3}{2}}}{\mathcal{N}^{\pm,\frac{3}{2}}_{\ell,n}(1+|\mathfrak{z}|^2)^{\frac{3}{2}}}\Big[[\mathfrak{z}^3+\ell(-1)^n\mathrm{c}]\exp\Big(-i\,\frac{3\widetilde{\lambda}}{2}\,\mathrm{Im}(\alpha)\Big)\mathcal{S}_n\Big(\alpha+\frac{3\widetilde{\lambda}}{2},\xi\Big)$$
$$+\ell[1-\ell(-1)^n\mathrm{c}\,\mathfrak{z}^3]\exp\Big(i\,\frac{3\widetilde{\lambda}}{2}\,\mathrm{Im}(\alpha)\Big)\mathcal{S}_n\Big(\alpha-\frac{3\widetilde{\lambda}}{2},\xi\Big)+\sqrt{3}\,\Gamma^{(\pm)}_{\ell}[\mathfrak{z}^2-\ell(-1)^n\mathrm{c}\,\mathfrak{z}]$$
$$\times\exp\Big(-i\,\frac{\widetilde{\lambda}}{2}\,\mathrm{Im}(\alpha)\Big)\mathcal{S}_n\Big(\alpha+\frac{\widetilde{\lambda}}{2},\xi\Big)+\ell\sqrt{3}\,\Gamma^{(\pm)}_{\ell}\big[\mathfrak{z}+\ell(-1)^n\mathrm{c}\,\mathfrak{z}^2\big]\exp\Big(i\,\frac{\widetilde{\lambda}}{2}\,\mathrm{Im}(\alpha)\Big)\mathcal{S}_n\Big(\alpha-\frac{\widetilde{\lambda}}{2},\xi\Big)\Big]. \tag{B6}$$

The evolution of the state (B5) now readily yields the spin density matrix for the $s=\frac{3}{2}$ example:

$$\rho^{(\frac{3}{2})}_{\mathcal{Q}}(t)=\sum_{n,\tilde{n}=0}^{\infty}\begin{pmatrix}\mathrm{B}^{(2,2)}_{n,\tilde{n}}(t)\delta_{n\tilde{n}} & \mathrm{B}^{(2,1)}_{n,\tilde{n}}(t)\mathcal{G}_{\tilde{n}n}(-\widetilde{\lambda}) & \mathrm{B}^{(2,-1)}_{n,\tilde{n}}(t)\mathcal{G}_{\tilde{n}n}(-2\widetilde{\lambda}) & \mathrm{B}^{(2,-2)}_{n,\tilde{n}}(t)\mathcal{G}_{\tilde{n}n}(-3\widetilde{\lambda})\\ \mathrm{B}^{(1,2)}_{n,\tilde{n}}(t)\mathcal{G}_{\tilde{n}n}(\widetilde{\lambda}) & \mathrm{B}^{(1,1)}_{n,\tilde{n}}(t)\delta_{n\tilde{n}} & \mathrm{B}^{(1,-1)}_{n,\tilde{n}}(t)\mathcal{G}_{\tilde{n}n}(-\widetilde{\lambda}) & \mathrm{B}^{(1,-2)}_{n,\tilde{n}}(t)\mathcal{G}_{\tilde{n}n}(-2\widetilde{\lambda})\\ \mathrm{B}^{(-1,2)}_{n,\tilde{n}}(t)\mathcal{G}_{\tilde{n}n}(2\widetilde{\lambda}) & \mathrm{B}^{(-1,1)}_{n,\tilde{n}}(t)\mathcal{G}_{\tilde{n}n}(\widetilde{\lambda}) & \mathrm{B}^{(-1,-1)}_{n,\tilde{n}}(t)\delta_{n\tilde{n}} & \mathrm{B}^{(-1,-2)}_{n,\tilde{n}}(t)\mathcal{G}_{\tilde{n}n}(-\widetilde{\lambda})\\ \mathrm{B}^{(-2,2)}_{n,\tilde{n}}(t)\mathcal{G}_{\tilde{n}n}(3\widetilde{\lambda}) & \mathrm{B}^{(-2,1)}_{n,\tilde{n}}(t)\mathcal{G}_{\tilde{n}n}(2\widetilde{\lambda}) & \mathrm{B}^{(-2,-1)}_{n,\tilde{n}}(t)\mathcal{G}_{\tilde{n}n}(\widetilde{\lambda}) & \mathrm{B}^{(-2,-2)}_{n,\tilde{n}}(t)\delta_{n\tilde{n}}\end{pmatrix}, \tag{B7}$$

where the elements are expressed via the factorized structure

$$\mathrm{B}^{(\imath,\jmath)}_{n,\tilde{n}}(t)\equiv\mathcal{B}^{(\frac{3}{2})}_{\imath,n}(t)\mathcal{B}^{(\frac{3}{2})}_{\jmath,\tilde{n}}(t)^*,\quad \imath,\jmath\in\{\pm1,\pm2\} \tag{B8}$$

of the following linear combinations

$$\mathcal{B}^{(\frac{3}{2})}_{\pm1,n}(t)=\frac{\mathcal{A}^{+,\frac{3}{2}}_{1,n}(t)\Gamma^{(+)}_1}{\mathcal{N}^{+,\frac{3}{2}}_{1,n}}+\frac{\mathcal{A}^{-,\frac{3}{2}}_{1,n}(t)\Gamma^{(-)}_1}{\mathcal{N}^{-,\frac{3}{2}}_{1,n}}\pm\frac{\mathcal{A}^{+,\frac{3}{2}}_{-1,n}(t)\Gamma^{(+)}_{-1}}{\mathcal{N}^{+,\frac{3}{2}}_{-1,n}}\pm\frac{\mathcal{A}^{-,\frac{3}{2}}_{-1,n}(t)\Gamma^{(-)}_{-1}}{\mathcal{N}^{-,\frac{3}{2}}_{-1,n}},$$
$$\mathcal{B}^{(\frac{3}{2})}_{\pm2,n}(t)=\frac{\mathcal{A}^{+,\frac{3}{2}}_{1,n}(t)}{\mathcal{N}^{+,\frac{3}{2}}_{1,n}}+\frac{\mathcal{A}^{-,\frac{3}{2}}_{1,n}(t)}{\mathcal{N}^{-,\frac{3}{2}}_{1,n}}\pm\frac{\mathcal{A}^{+,\frac{3}{2}}_{-1,n}(t)}{\mathcal{N}^{+,\frac{3}{2}}_{-1,n}}\pm\frac{\mathcal{A}^{-,\frac{3}{2}}_{-1,n}(t)}{\mathcal{N}^{-,\frac{3}{2}}_{-1,n}} \tag{B9}$$

containing the time-dependent phases $\mathcal{A}^{\pm,\frac{3}{2}}_{\ell,n}(t)\equiv\mathcal{A}^{\pm,\frac{3}{2}}_{\ell,n}\exp(-iE^{\pm,\frac{3}{2}}_{\ell,n}t)$. The constraint $\mathrm{Tr}\rho^{(\frac{3}{2})}_{\mathcal{Q}}(t)=1$ is obeyed by the qudit-reduced density matrix (B7). For the $s=\frac{3}{2}$ example the composition of the qudit-reduced density matrix in the spherical tensor basis is also assembled by employing the constructions (B7) and (4.4):

$$\varrho^{\mathcal{Q}}_{kq}(t)\big|_{s=\frac{3}{2}}=\sqrt{\frac{2k+1}{(3-k)!(4+k)!}}\sum_{n,\tilde{n}=0}^{\infty}\Bigg(\delta_{n\tilde{n}}\delta_{q,0}\big[6\big(\mathrm{B}^{(2,2)}_{n,\tilde{n}}(t)+(-1)^k\mathrm{B}^{(-2,-2)}_{n,\tilde{n}}(t)\big)-2(k^2+k-3)$$
$$\times\big(\mathrm{B}^{(1,1)}_{n,\tilde{n}}(t)+(-1)^k\,\mathrm{B}^{(-1,-1)}_{n,\tilde{n}}(t)\big)\big]+\delta_{q,-1}\sqrt{\frac{(k+1)!}{(k-1)!}}\,\mathcal{G}_{\tilde{n}n}(\widetilde{\lambda})\,\big(2\sqrt{3}\,\mathrm{B}^{(1,2)}_{n,\tilde{n}}(t)$$
$$-(k^2+k-6)\mathrm{B}^{(-1,1)}_{n,\tilde{n}}(t)-(-1)^k\,2\sqrt{3}\,\mathrm{B}^{(-2,-1)}_{n,\tilde{n}}(t)\big)+\delta_{q,1}\sqrt{\frac{(k+1)!}{(k-1)!}}\,\mathcal{G}_{\tilde{n}n}(-\widetilde{\lambda})$$
$$\times\big(-2\sqrt{3}\,\mathrm{B}^{(2,1)}_{n,\tilde{n}}(t)-(-1)^k\,(k^2+k-6)\,\mathrm{B}^{(1,-1)}_{n,\tilde{n}}(t)+(-1)^k\,2\sqrt{3}\,\mathrm{B}^{(-1,-2)}_{n,\tilde{n}}(t)\big)$$
$$+\sqrt{3\frac{(k+2)!}{(k-2)!}}\big[\delta_{q,-2}\,\mathcal{G}_{\tilde{n}n}(2\widetilde{\lambda})\big(\mathrm{B}^{(-1,2)}_{n,\tilde{n}}(t)+(-1)^k\,\mathrm{B}^{(-2,1)}_{n,\tilde{n}}(t)\big)$$
$$+\delta_{q,2}\,\mathcal{G}_{\tilde{n}n}(-2\widetilde{\lambda})\big(\mathrm{B}^{(2,-1)}_{n,\tilde{n}}(t)+(-1)^k\,\mathrm{B}^{(1,-2)}_{n,\tilde{n}}(t)\big)\big]+\sqrt{\frac{(k+3)!}{(k-3)!}}$$
$$\times\big((-1)^k\,\delta_{q,3}\,\mathcal{G}_{\tilde{n}n}(-3\widetilde{\lambda})\mathrm{B}^{(2,-2)}_{n,\tilde{n}}(t)+\delta_{q,-3}\,\mathcal{G}_{\tilde{n}n}(3\widetilde{\lambda})\,\mathrm{B}^{(-2,2)}_{n,\tilde{n}}(t)\big)\Bigg). \tag{B10}$$

APPENDIX C: QUASIPROBABILITY DISTRIBUTIONS FOR $s=\frac{3}{2}$

We now concisely list the analytic expressions for the quasiprobability densities in the phase space for the spin $s=\frac{3}{2}$ case with the following objective in mind. The generalized spin kitten configurations for higher values of s admit more extensive superposition of states existing in a larger Hilbert space. Consequently, spin kitten type states with increasingly complex

phase-space structures possessing, say, multiple peaks are likely to appear for larger s. The $s = \frac{3}{2}$ spin phase-space quasiprobability distributions following from (4.8), (4.11), and (4.13) read as follows:

$$\begin{aligned}
\mathrm{P}_{\mathcal{Q}}^{(\frac{3}{2})}(\theta,\phi) = \frac{1}{32\pi}\sum_{n,\tilde{n}=0}^{\infty}\big\{&(18-45\cos\theta+30\cos 2\theta-35\cos 3\theta)\,\mathrm{B}_{n,\tilde{n}}^{(2,2)}(t)\,\delta_{n\tilde{n}}+(18+45\cos\theta\\
&+30\cos 2\theta+35\cos 3\theta)\mathrm{B}_{n,\tilde{n}}^{(-2,-2)}(t)\delta_{n\tilde{n}}+(-2+55\cos\theta-30\cos 2\theta+105\cos 3\theta)\\
&\times\mathrm{B}_{n,\tilde{n}}^{(1,1)}(t)\,\delta_{n\tilde{n}}-(2+55\cos\theta+30\cos 2\theta+105\cos 3\theta)\,\mathrm{B}_{n,\tilde{n}}^{(-1,-1)}(t)\,\delta_{n\tilde{n}}+10\sqrt{3}(3\sin\theta\\
&-4\sin 2\theta+7\sin 3\theta)\mathrm{Re}\big(\exp(i\phi)\mathrm{B}_{n,\tilde{n}}^{(2,1)}(t)\mathcal{G}_{\tilde{n}n}(-\widetilde{\lambda})\big)+40\sqrt{3}(1-7\cos\theta)\sin^2\theta\\
&\times\mathrm{Re}\big(\exp(2i\phi)\mathrm{B}_{n,\tilde{n}}^{(2,-1)}(t)\mathcal{G}_{\tilde{n}n}(-2\widetilde{\lambda})\big)+280\sin^3\theta\,\mathrm{Re}\big(\exp(3i\phi)\mathrm{B}_{n,\tilde{n}}^{(2,-2)}(t)\\
&\times\mathcal{G}_{\tilde{n}n}(-3\widetilde{\lambda})\big)-10(\sin\theta+21\sin 3\theta)\,\mathrm{Re}\big(\exp(i\phi)\mathrm{B}_{n,\tilde{n}}^{(1,-1)}(t)\mathcal{G}_{\tilde{n}n}(-\widetilde{\lambda})\big)\\
&+40\sqrt{3}(1+7\cos\theta)\sin^2\theta\,\mathrm{Re}\big(\exp(2i\phi)\mathrm{B}_{n,\tilde{n}}^{(1,-2)}(t)\mathcal{G}_{\tilde{n}n}(-2\widetilde{\lambda})\big)+10\sqrt{3}(3\sin\theta\\
&+4\sin 2\theta+7\sin 3\theta)\mathrm{Re}\big(\exp(i\phi)\mathrm{B}_{n,\tilde{n}}^{(-1,-2)}(t)\mathcal{G}_{\tilde{n}n}(-\widetilde{\lambda})\big)\big\},
\end{aligned}\tag{C1}$$

$$\begin{aligned}
\mathrm{W}_{\mathcal{Q}}^{(\frac{3}{2})}(\theta,\phi) = \frac{1}{160\pi}\sum_{n,\tilde{n}=0}^{\infty}\big\{&\big(3(8\sqrt{15}+\sqrt{35})\cos\theta+5(8+2\sqrt{5}+6\sqrt{5}\cos 2\theta+\sqrt{35}\cos 3\theta)\big)\\
&\times\mathrm{B}_{n,\tilde{n}}^{(2,2)}(t)\delta_{n\tilde{n}}+\big(-3(8\sqrt{15}+\sqrt{35})\cos\theta+5(8+2\sqrt{5}+6\sqrt{5}\cos 2\theta-\sqrt{35}\cos 3\theta)\big)\\
&\times\mathrm{B}_{n,\tilde{n}}^{(-2,-2)}(t)\delta_{n\tilde{n}}+\big((8\sqrt{15}-9\sqrt{35})\cos\theta-5(-8+2\sqrt{5}+6\sqrt{5}\cos 2\theta\\
&+3\sqrt{35}\cos 3\theta)\big)\mathrm{B}_{n,\tilde{n}}^{(1,1)}(t)\delta_{n\tilde{n}}+\big((-8\sqrt{15}+9\sqrt{35})\cos\theta+5(8-2\sqrt{5}-6\sqrt{5}\cos 2\theta\\
&+3\sqrt{35}\cos 3\theta)\big)\mathrm{B}_{n,\tilde{n}}^{(-1,-1)}(t)\delta_{n\tilde{n}}+4\sqrt{5}\big(3(4+\sqrt{21})+20\sqrt{3}\cos\theta+5\sqrt{21}\cos 2\theta\big)\\
&\times\sin\theta\,\mathrm{Re}\big(\exp(i\phi)\mathrm{B}_{n,\tilde{n}}^{(2,1)}(t)\mathcal{G}_{\tilde{n}n}(-\widetilde{\lambda})\big)+40\sqrt{15}(1+\sqrt{7}\cos\theta)\sin^2\theta\\
&\times\mathrm{Re}\big(\exp(2i\phi)\mathrm{B}_{n,\tilde{n}}^{(2,-1)}(t)\mathcal{G}_{\tilde{n}n}(-2\widetilde{\lambda})\big)+40\sqrt{35}\sin^3\theta\,\mathrm{Re}\big(\exp(3i\phi)\mathrm{B}_{n,\tilde{n}}^{(2,-2)}(t)\mathcal{G}_{\tilde{n}n}(-3\widetilde{\lambda})\big)\\
&+8\sqrt{5}(4\sqrt{3}+3\sqrt{7}-15\sqrt{7}\cos^2\theta)\sin\theta\,\mathrm{Re}\big(\exp(i\phi)\mathrm{B}_{n,\tilde{n}}^{(1,-1)}(t)\mathcal{G}_{\tilde{n}n}(-\widetilde{\lambda})\big)\\
&+40\sqrt{15}(1-\sqrt{7}\cos\theta)\sin^2\theta\,\mathrm{Re}\big(\exp(2i\phi)\mathrm{B}_{n,\tilde{n}}^{(1,-2)}(t)\mathcal{G}_{\tilde{n}n}(-2\widetilde{\lambda})\big)+4\sqrt{5}[3(4+\sqrt{21})\\
&-20\sqrt{3}\cos\theta+5\sqrt{21}\cos 2\theta]\sin\theta\,\mathrm{Re}\big(\exp(i\phi)\mathrm{B}_{n,\tilde{n}}^{(-1,-2)}(t)\mathcal{G}_{\tilde{n}n}(-\widetilde{\lambda})\big)\big\},
\end{aligned}\tag{C2}$$

$$\begin{aligned}
\mathrm{Q}_{\mathcal{Q}}^{(\frac{3}{2})}(\theta,\phi) = \frac{1}{8\pi}\sum_{n,\tilde{n}=0}^{\infty}\Big\{&8\sin^6\left(\frac{\theta}{2}\right)\mathrm{B}_{n,\tilde{n}}^{(2,2)}(t)\delta_{n\tilde{n}}+24\sin^4\left(\frac{\theta}{2}\right)\cos^2\left(\frac{\theta}{2}\right)\mathrm{B}_{n,\tilde{n}}^{(1,1)}(t)\delta_{n\tilde{n}}+24\cos^4\left(\tfrac{\theta}{2}\right)\sin^2\left(\tfrac{\theta}{2}\right)\\
&\times\mathrm{B}_{n,\tilde{n}}^{(-1,-1)}(t)\delta_{n\tilde{n}}+8\cos^6\left(\frac{\theta}{2}\right)\mathrm{B}_{n,\tilde{n}}^{(-2,-2)}(t)\delta_{n\tilde{n}}+8\sqrt{3}\sin\theta\sin^4\left(\frac{\theta}{2}\right)\mathrm{Re}\Big(\exp(-i\phi)\\
&\times\mathrm{B}_{n,\tilde{n}}^{(1,2)}(t)\mathcal{G}_{\tilde{n}n}(\widetilde{\lambda})\Big)+8\sqrt{3}\sin\theta\cos^4\left(\tfrac{\theta}{2}\right)\mathrm{Re}\big(\exp(-i\phi)\mathrm{B}_{n,\tilde{n}}^{(-2,-1)}(t)\mathcal{G}_{\tilde{n}n}(\widetilde{\lambda})\big)\\
&+4\sqrt{3}\sin^2\theta\sin^2\left(\frac{\theta}{2}\right)\mathrm{Re}\big(\exp(-2i\phi)\mathrm{B}_{n,\tilde{n}}^{(-1,2)}(t)\mathcal{G}_{\tilde{n}n}(2\widetilde{\lambda})\big)+4\sqrt{3}\sin^2\theta\cos^2\left(\frac{\theta}{2}\right)\\
&\times\mathrm{Re}\big(\exp(-2i\phi)\mathrm{B}_{n,\tilde{n}}^{(-2,1)}(t)\mathcal{G}_{\tilde{n}n}(2\widetilde{\lambda})\big)+6\sin^3\theta\,\mathrm{Re}\big(\exp(-i\phi)\mathrm{B}_{n,\tilde{n}}^{(-1,1)}(t)\mathcal{G}_{\tilde{n}n}(\widetilde{\lambda})\big)\\
&+2\sin^3\theta\,\mathrm{Re}\big(\exp(-3i\phi)\mathrm{B}_{n,\tilde{n}}^{(-2,2)}(t)\mathcal{G}_{\tilde{n}n}(3\widetilde{\lambda})\big)\Big\}.
\end{aligned}\tag{C3}$$

Similar to the observation in Sec. IV A the above qudit quasiprobability distributions follow from the corresponding bipartite structures via an integration over the oscillator phase space. Our descriptions of the generalized kitten states (Sec. VI A) and other localized spin states (Sec. V) for the $s = \frac{3}{2}$ example are based on the structure (C1)–(C3) outlined above.

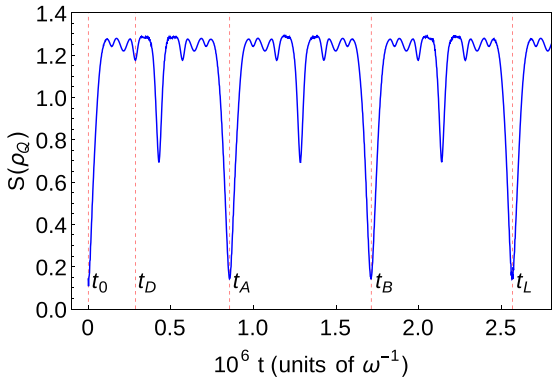

FIG. 10. For $s = \frac{3}{2}$ case we assume $c = i$ in (3.1), and maintain other parameters in Fig. 4(a) unaltered. The qudit entropy returns, at its local minima ($t_A = 0.856\,011 \times 10^6$, $t_B = 1.711\,003 \times 10^6$, $t_L = 2.564\,398 \times 10^6$) to the configuration $S(\rho_Q) \ll 1$. The respective Hilbert-Schmidt distances of these configurations from the initial state read as $d_{HS}|_{t_A} = 1.062\,185$, $d_{HS}|_{t_B} = 1.050\,424$, $d_{HS}|_{t_L} = 0.012\,075$. As argued previously, generalized spin kitten states develop at t_A and t_B, while at t_L the system nearly returns to its original state. On the other hand, at the local minimum indicated by $t_D = 0.284\,499 \times 10^6$ the entropy behaves as $S(\rho_Q)|_{t_D} \lesssim O(\ln 4)$. Consequently, a localized state with a largely mixed density matrix forms at t_D.

In particular, the generalized three-kitten states emerge at times t_A and t_B in Fig. 5.

APPENDIX D: PHASE-SPACE DENSITIES FOR INITIALLY ENTANGLED STATES

In this work so far we have considered factorized initial state characterized by $c = 0$ in (3.1), and studied the time evolution of the system by employing the P_Q representation. Here, we briefly consider bipartite initial states which are entangled. We also comment on the relative utility of different qudit quasiprobability distributions in the present problem. In particular, for spin $s = \frac{3}{2}$ case we choose $c = i$ in the initial state (3.1) while retaining other parametric values listed in Fig. 4(a) unchanged. The resulting evolution of entropy (Fig. 10) indicates that the composite system approximately returns (5.4) to its initial state at t_L. Based on the earlier discussions, we note that the generalized spin kitten states are produced at t_A and t_B. A numerical reconstruction of the state at t_A is given in Table III. The general features of the evolution of entropy in Fig. 10 are similar to those in Fig. 4(a). Comparing the diagrams in Figs. 11(a_1)–11(a_3) we note that for the phase-space description of the largely pure generalized spin kitten states, the P_Q representation [Fig. 11(a_1)] appears to be most suitable tool for characterization of the state as it, compared to the other distributions, embodies maximum variation in the phase-space density. On the other hand, the illustrations in Figs. 11(b_1)–11(b_3) indicate that the phase-space description of the localized mixed qudit states are more robust in the sense that the broad characteristics of all distributions (P_Q, W_Q, Q_Q) are qualitatively similar.

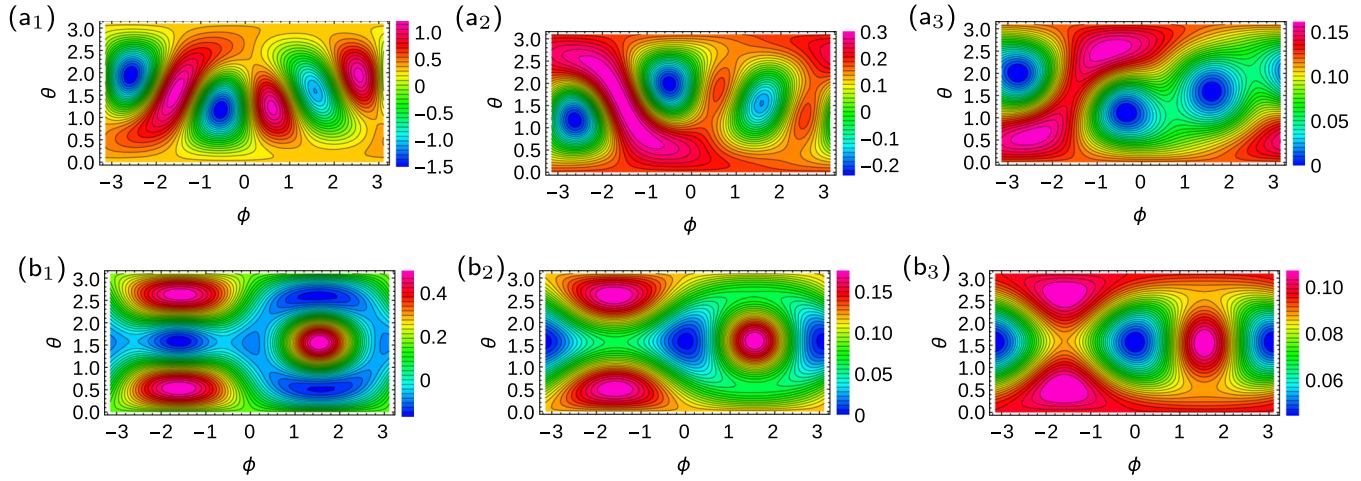

FIG. 11. The diagrams (a_1), (a_2), and (a_3) study, respectively, the spin quasiprobability densities P_Q, W_Q, Q_Q for the generalized spin kitten state at t_A (Fig. 10). The remaining diagrams (b_1), (b_2), and (b_3) illustrate the said P_Q, W_Q, Q_Q distributions realized at t_D (Fig. 10) for the mixed qudit state endowed with locally minimum but substantially large value of the entropy.

[1] E. T. Jaynes and F. W. Cummings, Proc. IEEE **51**, 89 (1963).

[2] A. D. Armour, M. P. Blencowe, and K. C. Schwab, Phys. Rev. Lett. **88**, 148301 (2002).

[3] M. D. LaHaye, J. Suh, P. M. Echternach, K. C. Schwab, and M. L. Roukes, Nat. Lett. **459**, 960 (2009).

[4] T. Niemczyk, F. Deppe, H. Huebl, E. P. Menzel, F. Hocke, M. J. Schwarz, J. J. Garcia-Ripoli, D. Zueco, T. Hümer, E. Solano, A. Marx, and R. Gross, Nat. Phys. **6**, 772 (2010).

[5] P. Forn-Díaz, J. Lisenfeld, D. Marcos, J. J. García-Ripoll, E. Solano, C. J. P. M. Harmans, and J. E. Mooij, Phys. Rev. Lett. **105**, 237001 (2010).

[6] A. A. Anappara, S. De Liberato, A. Tredicucci, C. Ciuti, G. Biasiol, L. Sorba, and F. Beltram, Phys. Rev. B **79**, 201303(R) (2009).

[7] Y. Todorov, A. M. Andrews, R. Colombelli, S. De Liberato, C. Ciuti, P. Klang, G. Strasser, and C. Sirtori, Phys. Rev. Lett. **105**, 196402 (2010).

[8] J. Q. You and F. Nori, Phys. Today **58**(11), 42 (2005).
[9] J. Q. You and F. Nori, Nature (London) **474**, 589 (2011).
[10] P. D. Nation, J. R. Johansson, M. P. Blencowe, and F. Nori, Rev. Mod. Phys. **84**, 1 (2012).
[11] I. Buluta, S. Ashhab, and F. Nori, Rep. Prog. Phys. **74**, 104401 (2011).
[12] I. Buluta and F. Nori, Science **326**, 108 (2009).
[13] I. M. Georgescu, S. Ashhab, and F. Nori, Rev. Mod. Phys. **86**, 153 (2014).
[14] N. Lambert, Y. Matsuzaki, K. Kakuyanagi, N. Ishida, S. Saito, and F. Nori, Phys. Rev. B **94**, 224510 (2016).
[15] E. O. Kiktenko, A. K. Fedorov, O. V. Man'ko, and V. I. Man'ko, Phys. Rev. A **91**, 042312 (2015).
[16] R. Lapkiewicz, P. Li, C. Schäff, N. K. Langford, S. Ramelow, M. Wieśniak, and A. Zeilinger, Nature (London) **474**, 490 (2011).
[17] Z.-L. Xiang, S. Ashhab, J. Q. You, and F. Nori, Rev. Mod. Phys. **85**, 623 (2013).
[18] J. M. Radcliffe, J. Phys. A: Math. Gen. **4**, 313 (1971).
[19] F. T. Arecchi, E. Courtens, R. Gilmore, and H. Thomas, Phys. Rev. A **6**, 2211 (1972).
[20] G. S. Agarwal and S. S. Trivedi, Opt. Commun. **18**, 417 (1976).
[21] D. Braun, P. A. Braun, and F. Haake, Opt. Commun. **179**, 411 (2000).
[22] O. Castaños, E. Nahmad-Achar, R. Lopez-Peña, and J. G. Hirsch, Phys. Rev. A **84**, 013819 (2011).
[23] G. S. Agarwal, A. C. Brown, L. M. Narducci, and G. Vetri, Phys. Rev. A **15**, 1613 (1977).
[24] P. D. Drummond and S. S. Hassan, Phys. Rev. A **22**, 662 (1980).
[25] S. Haroche and J.-M. Raimond, *Exploring the Quantum: Atoms, Cavities, and Photons* (Oxford University Press, Oxford, 2006).
[26] G. S. Agarwal, R. R. Puri, and R. P. Singh, Phys. Rev. A **56**, 2249 (1997).
[27] C. C. Gerry and R. Grobe, Phys. Rev. A **56**, 2390 (1997).
[28] D. Leibfried, E. Knill, S. Seidelin, J. Britton, R. B. Blakestad, J. Chiaverini, D. B. Hume, W. M. Itano, J. D. Jost, C. Langer, R. Ozeri, R. Reichle, and D. J. Wineland, Nature (London) **438**, 639 (2005).
[29] R. McConnell, H. Zhang, S. Ćuk, J. Hu, M. H. Schleier-Smith, and V. Vuletić, Phys. Rev. A **88**, 063802 (2013).
[30] T. Chalopin, C. Bouazza, A. Evrard, V. Makhalov, D. Dreon, J. Dalibard, L. A. Sidorenkov, and S. Nascimbene, Nat. Commun. **9**, 1 (2018).
[31] C. Song, K. Xu, H. Li, Y. R. Zhang, X. Zhang, W. Liu, Q. Guo, Z. Wang, W. Ren, J. Hao, H. Feng, H. Fan, D. Zheng, D. W. Wang, H. Wang, and S. Y. Zhu, Science **365**, 574 (2019).
[32] M. Kitagawa and M. Ueda, Phys. Rev. Lett. **67**, 1852 (1991).
[33] D. J. Wineland, J. J. Bollinger, W. M. Itano, F. L. Moore, and D. J. Heinzen, Phys. Rev. A **46**, R6797(R) (1992).
[34] M. Kitagawa and M. Ueda, Phys. Rev. A **47**, 5138 (1993).
[35] A. Miranowicz, S. K. Özdemir, Yu-xi Liu, M. Koashi, N. Imoto, and Y. Hirayama, Phys. Rev. A **65**, 062321 (2002).
[36] T.-L. Wang, L.-N. Wu, W. Yang, G.-R. Jin, N. Lambert, and F. Nori, New J. Phys. **16**, 063039 (2014).
[37] L. Song, X. Wang, D. Yan, and Z. Zong, J. Phys. B: At., Mol. Opt. Phys. **39**, 559 (2006).
[38] J. I. Cirac, M. Lewenstein, K. Mølmer, and P. Zoller, Phys. Rev. A **57**, 1208 (1998).
[39] Y. Jing, M. Fadel, V. Ivannikov, and T. Byrnes, New J. Phys. **21**, 093038 (2019).
[40] D. Tsomokos, S. Ashhab, and F. Nori, New J. Phys. **10**, 113020 (2008).
[41] Y. Zhang, L. Yu, J.-Q. Liang, G. Chen, S. Jia, and F. Nori, Sci. Rep. **4**, 4083 (2014).
[42] V. Macrì, F. Nori, S. Savasta, and D. Zueco, Phys. Rev. A **101**, 053818 (2020).
[43] V. Petersen, L. B. Madsen, and K. Mølmer, Phys. Rev. A **71**, 012312 (2005).
[44] J. Hald, J. L. Sørensen, C. Schori, and E. S. Polzik, Phys. Rev. Lett. **83**, 1319 (1999).
[45] J. Ma, X. Wang, C. P. Sun, and F. Nori, Phys. Rep. **509**, 89 (2011).
[46] E. K. Irish, J. Gea-Banacloche, I. Martin, and K. C. Schwab, Phys. Rev. B **72**, 195410 (2005).
[47] S. Ashhab and F. Nori, Phys. Rev. A **81**, 042311 (2010).
[48] G. S. Agarwal, Phys. Rev. A **24**, 2889 (1981).
[49] C. L. Mehta, Phys. Rev. Lett. **18**, 752 (1967).
[50] C. Gerry and P. Knight, *Introductory Quantum Optics* (Cambridge University Press, Cambridge, 2005).
[51] V. I. Man'ko and O. V. Man'ko, J. Exp. Theor. Phys. **85**, 430 (1997).
[52] V. V. Dodonov and V. I. Man'ko, Phys. Lett. A **229**, 335 (1997).
[53] K. M. C. Lee and C. K. Law, Phys. Rev. A **88**, 015802 (2013).
[54] J. D. Talman, *Special Functions: A Group Theoretic Approach* (Benjamin, New York, 1968).
[55] E. C. G. Sudarshan, Phys. Rev. Lett. **10**, 277 (1963).
[56] H. Moya-Cessa and P. L. Knight, Phys. Rev. A **48**, 2479 (1993).
[57] J. P. Dowling, G. S. Agarwal, and W. P. Schleich, Phys. Rev. A **49**, 4101 (1994).
[58] G. E. Andrews, R. Askey, and R. Roy, *Special Functions* (Cambridge University Press, Cambridge, 1999).
[59] J. Meixner, Math. Z. **44**, 531 (1939).
[60] H. Araki and E. H. Lieb, Commun. Math. Phys. **18**, 160 (1970).
[61] V. V. Dodonov, O. V. Man'ko, V. I. Man'ko, A. Wünsche, J. Mod. Opt. **47**, 633 (2000).
[62] E. Romera and F. de los Santos, Phys. Rev. Lett. **99**, 263601 (2007).
[63] I. S. Averbukh and N. F. Perelman, Phys. Lett. A **139**, 449 (1989).
[64] A. Sugita and H. Aiba, Phys. Rev. E **65**, 036205 (2002).
[65] E. Romera, O. Castanõs, M. Calixto, and F. Pérz-Bernal, J. Stat. Mech. (2017) 013101.
[66] K. Wódkiewicz, Opt. Commun. **51**, 198 (1984).
[67] D. F. V. James and J. Jerke, Can. J. Phys. **85**, 625 (2007).
[68] G. M. D'Ariano, L. Maccone, and M. Paini, J. Opt. B **5**, 77 (2003).
[69] J. Teles, E. R. deAzevedo, R. Auccaise, R. S. Sarthour, I. S. Oliveira, and T. J. Bonagamba, J. Chem. Phys. **126**, 154506 (2007).
[70] Y. Wu, X. Li, L. M. Duan, D. G. Steel, and D. Gammon, Phys. Rev. Lett. **96**, 087402 (2006).
[71] D. Gross, Y.-K. Liu, S. T. Flammia, S. Becker, and J. Eisert, Phys. Rev. Lett. **105**, 150401 (2010).
[72] B. Chen, F. Zhou, L. Song, H. Shen, and N. Xu, Appl. Phys. Lett. **114**, 041102 (2019).
[73] S. Agarwal, S. M. Hashemi Rafsanjani, and J. H. Eberly, Phys. Rev. A **85**, 043815 (2012).